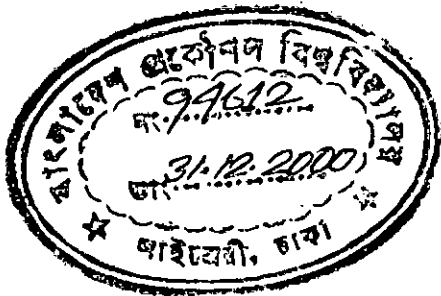


A STUDY OF THE QUANTIZATION EFFECTS IN MOS INVERSION LAYER USING AN IMPROVED APPROACH

A Thesis submitted to
the Department of Electrical and Electronic Engineering of BUET, Dhaka
in partial fulfillment of the requirements
for the degree of
Master of Science in Engineering
(Electrical and Electronic)



by

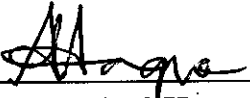
Md. Iqbal Bahar Chowdhury


December 2000





The thesis " A STUDY OF THE QUANTIZATION EFFECTS IN MOS INVERSION LAYER USING AN IMPROVED APPROACH" submitted by Md. Iqbal Bahar Chowdhury, Roll No. 9406221F, Registration No. 89177, Session 1993-94-95 to the Department of Electrical and Electronic Engineering, BUET has been accepted as satisfactory for partial fulfillment of the requirements for the degree of Master of Science in Engineering (Electrical and Electronic).

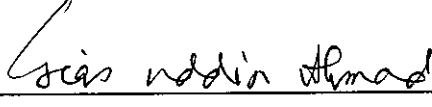
BOARD OF EXAMINERS

1. 

 2. 

 3. 

 4. 

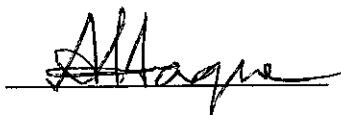
 5. 

- Dr. Anisul Haque**
Associate Professor
Department of Electrical and Electronic Engineering
BUET, Dhaka-1000, Bangladesh.
- Dr. Shahidul Islam Khan**
Professor and Head
Department of Electrical and Electronic Engineering
BUET, Dhaka-1000, Bangladesh.
- Dr. M. Rezwan Khan**
Professor
Department of Electrical and Electronic Engineering
BUET, Dhaka-1000, Bangladesh.
- Dr. A. H. M. Zahirul Alam**
Professor
Department of Electrical and Electronic Engineering
BUET, Dhaka-1000, Bangladesh.
- Dr. Gias uddin Ahmad**
Professor
Department of Physics
BUET, Dhaka-1000, Bangladesh.
- Chairman**
(Supervisor)
- Member**
(Ex-officio)
- Member**
- Member**
- Member**
(External)

DECLARATION

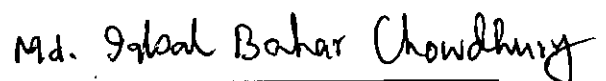
I hereby declare that this work has been done by me and it has not been submitted elsewhere for the award of any degree or diploma.

Countersigned:



(Dr. Anisul Haque)

Supervisor



(Md. Iqbal Bahar Chowdhury)

DEDICATION

This work is dedicated to my parents for their constant support, my wife for her sincere love, Meehal- my son- for his divine presence, and Biva and Rafa- my loving nieces- for their charming company.

ACKNOWLEDGEMENT

The author expresses his indebtedness, sincere gratitude and profound respect to his supervisor Dr. Anisul Haque, Associate Professor, Dept. of EEE, BUET, for his continuous guidance, suggestions and wholehearted supervision throughout the progress of this work, without which this thesis never be materialized.

The author is grateful to Mr. Fayyaz Khan, Head, Dept. of EEE, AUST, who provided with all the facilities of the department and co-operation to complete the work. In this regard, the author also likes to express thanks and gratitude to Dr. Shahidul Islam Khan, Professor and Head, Dept. of EEE, BUET.

The author is indebted to Dr. A. H. M. Zahirul Alam, Professor, Dept. of EEE, BUET, for providing with rare books and materials. The author also expresses thanks and gratitude to Dr. Md. Shah Alam, Dr. Kazi Mujibur Rahman and Dr. Md. Kamrul Hasan of Dept. of EEE, BUET, for their invaluable software support and helpful advice. Also the author gratefully recalls the spontaneous co-operation obtained from Mr. Khawza Ifterkher Uddin Ahmed, Mr. Golam Toaha Rasul, Mr. Murshed Mahmud Chowdhury and Mr. Saif Uz Zaman of Dept. of EEE, AUST.

Finally, the author would like to thank his borthers, sister and brother-in-law for their inspiration and encouragement throughout the progress of this work, which made the thesis a possible one.

ABSTRACT

With the scaling down of MOSFET feature size, quantum mechanical (QM) effects on these devices are becoming important. It is found that, due to quantization, carriers move a distance away from the Si/SiO_2 interface, which increases the effective gate oxide thickness and thereby affects the effective gate capacitance, inversion charge density, threshold voltage etc. Hence, an accurate modeling for such devices must be made to include these QM effects, which require calculation of eigenenergies and wavefunctions from Schrödinger's equation. Conventionally this calculation is done using a boundary condition, referred to as *conventional or zero boundary condition*, that assumes that wavefunctions vanish at the interface i.e. there is no wavefunction penetration inside the oxide region. Actually, the validity of zero boundary condition is not justified for the deep sub-micron ($\leq 30 \text{ \AA}$ gate oxide thickness) devices, as the error made is comparable to device dimensions. In such cases, for a more accurate modeling, the wavefunction penetration in the oxide should be taken into account.

This work calculates gate capacitances of deep submicron MOSFETs by considering wavefunction penetration in the oxide using a new *asymptotic boundary condition*. In this work, using both conventional and asymptotic boundary conditions, shift of DC charge centroid and gate capacitance are calculated. To reduce the computational complexity in QM calculations, a recently developed *Green's function formalism* along with *transmission line analogy* is employed. A comparison of the calculated results show that the results are dependent on the choice of boundary conditions. It is also seen that the choice of appropriate boundary condition becomes more important as the devices are scaled down with reduced oxide thickness and increased surface electric field.

Contents

| | |
|--|------------|
| DECLARATION | ii |
| DEDICATION | iii |
| ACKNOWLEDGEMENT | iv |
| ABSTRACT | v |
| | |
| 1 INTRODUCTION | 1 |
| 1.1 Literature Review | 3 |
| 1.2 Scope of the Work | 7 |
| 1.3 Organization of the Thesis | 8 |
| | |
| 2 REVIEW OF MOS THEORY: SEMI-CLASSICAL AND QUANTUM APPROACH | 9 |
| 2.1 Basic Structure | 10 |
| 2.2 Energy Band Diagram | 12 |
| 2.2.1 Zero Bias | 12 |
| 2.2.2 Positive Bias | 12 |
| 2.3 Semi-classical Approach | 16 |
| 2.4 Quantum Mechanical Approach | 21 |
| 2.4.1 Basic Formulation | 21 |
| 2.4.2 Approximate Techniques of QM Solution | 24 |
| 2.4.2.1 Airy Function Approximation | 25 |
| 2.4.2.2 Variational Approach | 25 |

| | | |
|----------|--|-----------|
| 3 | TRANSMISSION LINE ANALOGY AND GREEN'S FUNCTION FORMALISM: AN OVERVIEW | 27 |
| 3.1 | Transmission Line Analogy | 28 |
| 3.2 | Green's Function Formalism | 31 |
| 4 | RESULTS AND DISCUSSION | 34 |
| 4.1 | Potential Profile | 35 |
| 4.2 | General Effects of the Boundary Conditions | 37 |
| 4.3 | Effects of Variation of Oxide Thickness | 46 |
| 4.4 | Effects of Variation of Surface Electric Field | 48 |
| 4.5 | Effects of Variation of Gate Voltage | 52 |
| 5 | CONCLUSION | 63 |
| 5.1 | Discussion | 64 |
| 5.2 | Suggestions for Future Work | 64 |
| | Bibliography | 66 |

List of Figures

| | | |
|-----|--|----|
| 2.1 | An enhancement type n-channel MOS transistor. | 11 |
| 2.2 | Energy band diagram for zero bias condition assuming $\Phi_m = \Phi_{si}$ for p-type substrate. | 13 |
| 2.3 | Energy band diagram for zero bias condition assuming $\Phi_m = \Phi_{si}$ for n-type substrate. | 13 |
| 2.4 | Energy band diagram under depletion condition. | 15 |
| 2.5 | Energy band diagram under strong inversion condition. | 15 |
| 2.6 | Energy band diagram at flat band condition ($\Phi_{ms} \neq 0$). | 17 |
| 2.7 | Energy band diagram at onset of strong inversion condition. | 17 |
| 3.1 | A potential barrier with an incident electron (solid line) and the reflected wave (dashed line). | 29 |
| 4.1 | Surface Potential, ϕ_s vs. Surface Electric Field, F_s , with Doping Concentrations, $N_A = 1 \times 10^{17} \text{ cm}^{-3}$, $N_A = 5 \times 10^{17} \text{ cm}^{-3}$ and $N_A = 10 \times 10^{17} \text{ cm}^{-3}$ and oxide thickness, $T_{OX} = 20 \text{ \AA}$. Here, $T = 300^0 \text{ K}$ | 36 |
| 4.2 | Potential profile for $F_s = 0.75 \text{ MV/cm}$ and 1.5 MV/cm . Doping concentration, $N_A = 5 \times 10^{17} \text{ cm}^{-3}$, Oxide thickness, $T_{OX} = 20 \text{ \AA}$, $T = 300^0 \text{ K}$. The interface is at 0 \AA | 38 |
| 4.3 | First Three Wavefunctions (normalized) for both boundary conditions with $F_s = 0.75$ and $F_s = 1.5 \text{ MV/cm}$. Doping concentration = $5 \times 10^{17} \text{ cm}^{-3}$, Oxide thickness= 20 \AA , $T = 300^0 \text{ K}$. The interface is at 0 \AA | 41 |

| | | |
|------|--|----|
| 4.4 | Inversion charge density for three lowest eigenenergies for both boundary conditions with $F_s = 0.75$ MV/cm and 1.5 MV/cm. Doping concentration = $5 \times 10^{17} \text{ cm}^{-3}$, Oxide thickness=20 Å, $T = 300^0 \text{ K}$. The interface is at 0 Å. | 43 |
| 4.5 | Variation of three lowest eigenenergies with respect to Fermi energy level against surface electric field, F_s for both boundary conditions. Doping concentration = $5 \times 10^{17} \text{ cm}^{-3}$, Oxide thickness=20 Å, $T = 300^0 \text{ K}$ | 44 |
| 4.6 | Total Inversion charge density for both boundary conditions with $F_s = 0.75$ MV/cm and 1.5 MV/cm. Doping concentration = $5 \times 10^{17} \text{ cm}^{-3}$, Oxide thickness=20 Å, $T = 300^0 \text{ K}$. The interface is at 0 Å | 45 |
| 4.7 | DC Charge Centroid shift from the interface, X_{DC} vs. Oxide Thickness, T_{OX} , with Doping Concentrations, $N_A = 1 \times 10^{17} \text{ cm}^{-3}$, $N_A = 5 \times 10^{17} \text{ cm}^{-3}$ and $N_A = 10 \times 10^{17} \text{ cm}^{-3}$. $T = 300^0 \text{ K}$ | 49 |
| 4.8 | Effective gate oxide capacitance, C_{EFF} vs. Oxide Thickness, T_{OX} , with Doping Concentrations, $N_A = 1 \times 10^{17} \text{ cm}^{-3}$, $N_A = 5 \times 10^{17} \text{ cm}^{-3}$ and $N_A = 10 \times 10^{17} \text{ cm}^{-3}$. $T = 300^0 \text{ K}$ | 50 |
| 4.9 | First eigenenergy with respect to Si potential energy at the interface, E_1 vs. Surface Electric Field, F_s , with Doping Concentrations, $N_A = 1 \times 10^{17} \text{ cm}^{-3}$, $N_A = 5 \times 10^{17} \text{ cm}^{-3}$ and $N_A = 10 \times 10^{17} \text{ cm}^{-3}$. $T = 300^0 \text{ K}$ | 53 |
| 4.10 | Second eigenenergy with respect to Si potential energy at the interface, E_2 vs. Surface Electric Field, F_s , with Doping Concentrations, $N_A = 1 \times 10^{17} \text{ cm}^{-3}$, $N_A = 5 \times 10^{17} \text{ cm}^{-3}$ and $N_A = 10 \times 10^{17} \text{ cm}^{-3}$. $T = 300^0 \text{ K}$ | 54 |
| 4.11 | Third eigenenergy with respect to Si potential energy at the interface, E_3 vs. Surface Electric Field, F_s , with Doping Concentrations, $N_A = 1 \times 10^{17} \text{ cm}^{-3}$, $N_A = 5 \times 10^{17} \text{ cm}^{-3}$ and $N_A = 10 \times 10^{17} \text{ cm}^{-3}$. $T = 300^0 \text{ K}$ | 55 |
| 4.12 | Inversion Charge Carrier Density, N_{inv} vs. Surface Electric Field, F_s , with Doping Concentrations, $N_A = 1 \times 10^{17} \text{ cm}^{-3}$, $N_A = 5 \times 10^{17} \text{ cm}^{-3}$ and $N_A = 10 \times 10^{17} \text{ cm}^{-3}$. $T = 300^0 \text{ K}$ | 56 |

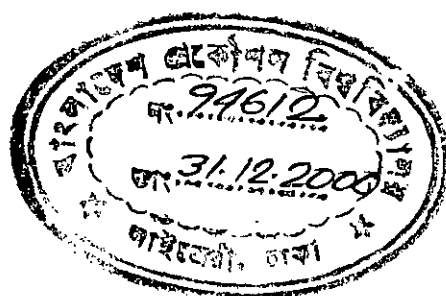
| | |
|--|----|
| 4.13 DC Charge Centroid Shift from the interface, X_{DC} vs. Surface Electric Field, F_s , with Doping Concentrations, $N_A = 1 \times 10^{17} \text{ cm}^{-3}$, $N_A = 5 \times 10^{17} \text{ cm}^{-3}$ and $N_A = 10 \times 10^{17} \text{ cm}^{-3}$. $T = 300^0 \text{ K}$ | 57 |
| 4.14 Effective Gate Capacitance, C_{EFF} vs. Surface Electric Field, F_s , with Doping Concentrations, $N_A = 1 \times 10^{17} \text{ cm}^{-3}$, $N_A = 5 \times 10^{17} \text{ cm}^{-3}$ and $N_A = 10 \times 10^{17} \text{ cm}^{-3}$. $T = 300^0 \text{ K}$ | 58 |
| 4.15 Inversion Charge Carrier Density, N_{inv} vs. Gate Voltage, V_G , with Doping Concentrations, $N_A = 1 \times 10^{17} \text{ cm}^{-3}$, $N_A = 5 \times 10^{17} \text{ cm}^{-3}$ and $N_A = 10 \times 10^{17} \text{ cm}^{-3}$. $T = 300^0 \text{ K}$ | 60 |
| 4.16 DC Charge Centroid Shift from the interface, X_{DC} vs. Gate Voltage, V_G , with Doping Concentrations, $N_A = 1 \times 10^{17} \text{ cm}^{-3}$, $N_A = 5 \times 10^{17} \text{ cm}^{-3}$ and $N_A = 10 \times 10^{17} \text{ cm}^{-3}$. $T = 300^0 \text{ K}$ | 61 |
| 4.17 Effective Gate Capacitance, C_{EFF} vs. Gate Voltage, V_G , with Doping Concentrations, $N_A = 1 \times 10^{17} \text{ cm}^{-3}$, $N_A = 5 \times 10^{17} \text{ cm}^{-3}$ and $N_A = 10 \times 10^{17} \text{ cm}^{-3}$. $T = 300^0 \text{ K}$ | 62 |

List of Tables

| | | |
|-----|--|----|
| 4.1 | Calculated eigenenergies, E_n with respect to Si potential energy at the interface for both boundary conditions with $F_s = 0.75$ MV/cm and 1.5 MV/cm. Doping concentration, $N_A = 5 \times 10^{17} \text{ cm}^{-3}$, Oxide thickness, $T_{OX} = 20 \text{ \AA}$, $T = 300^0 \text{ K}$ | 39 |
| 4.2 | Calculated DC charge centroid shift from the interface, X_{DC} for both boundary conditions with $F_s = 0.75$ MV/cm and 1.5 MV/cm. Doping concentration, $N_A = 5 \times 10^{17} \text{ cm}^{-3}$, Oxide thickness, $T_{OX} = 20 \text{ \AA}$, $T = 300^0 \text{ K}$ | 47 |
| 4.3 | Calculated effective gate capacitance, C_{EFF} for both boundary conditions with $F_s = 0.75$ MV/cm and 1.5 MV/cm. Doping concentration, $N_A = 5 \times 10^{17} \text{ cm}^{-3}$, Oxide thickness, $T_{OX} = 20 \text{ \AA}$, $T = 300^0 \text{ K}$ | 47 |

Chapter 1

INTRODUCTION



In order to obtain lower chip area i.e. higher level of integration, and higher speed of operation, the current trend of MOSFET fabrication is to increasingly scale down the device feature size. But with the advancement of miniaturization of MOSFET feature size, channel lengths approach deep submicron dimensions. This results in successively lower gate oxide thickness (T_{OX}) and higher levels of channel doping concentration (N_{SUB}) in order to simultaneously satisfy the need for desired device turn-off and drive-current capabilities guided by the rules of scaling methodology [1]. According to the National Technological Roadmap for Semiconductors (NTRS) [2], the scaling trend is such that T_{OX} approaches to less than 2.0 nm for a sub-100 nm generation device; on the other hand N_{SUB} must be at least equal to $10 \times 10^{18} \text{ cm}^{-3}$ so that short channel effects can be minimized.

In deep submicron ($\leq 0.25 \mu\text{m}$ gate length) technology, the combination of extremely thin oxide ($T_{OX} \leq 10 \text{ nm}$) and high channel doping concentration ($N_{SUB} \geq 10^{17} \text{ cm}^{-3}$) results in very high transverse electric fields at the Si/SiO₂ interface [1]. The electric field is sufficiently high, even near the threshold of inversion, to bend the energy bands at the interface significantly. With this band bending, the potential well becomes sufficiently narrow and steep to quantize the motion of inversion layer carriers in the direction normal to the interface. As a result, energy levels are split into subbands (2-D density of states) in such a manner that the lowest allowed energy level for electrons in the well does not coincide with the bottom of the conduction band. Each of these subbands correspond to a quantized level for motion in the direction normal to the interface, with a continuum for motion parallel to the surface. These quantum mechanical (QM) effects are manifested through measurable device parameters such as inversion layer charge density and resistance, threshold voltage, and the oxide thickness extracted from capacitance vs. voltage (C-V) or Fowler-Nordheim tun-

neling current measurements. Modeling of these QM effects are important in deep submicron device design. The use of traditional, or semi-classical, models in device analysis and design, in which these effects are neglected, is inadequate at deep submicron dimensions and will lead to erroneous and misleading predictions of the device structure and electrical behaviour, such as the physical oxide thickness, threshold voltage, drive current, capacitance, on-state series resistance, and the polysilicon work function.

From the above discussion it is pointed out that an accurate physical description, including QM effects, of charge distribution in inversion layer formed at Si/SiO₂ interface due to large transverse field caused by gate bias becomes increasingly important with decreasing MOSFET feature size. If semi-classical picture of this charge distribution is used, accurate determination of gate oxide thickness is not possible for submicron devices. From the QM viewpoint, carriers actually move some distance away from the interface due to the quantization of carrier energy states and thus leads to an increase of gate oxide thickness which is significant in deep submicron dimensions. This, therefore, results in increased threshold voltage and decreased gate capacitance.

1.1 Literature Review

In order to estimate various QM effects, it is necessary to calculate the energies of the quantized states and the corresponding wave functions. Stern and Howard [3] first considered this treatment and solved Schrödinger's equation mostly concerning with the lowest levels of subbands split up from the conduction band. They assumed the potential profile near the interface as triangular and calculated wave functions from the variational principle. Later Stern [4] solved the self-consistent solution of Schrödinger's and Poisson's equations. He calculated the wave functions assuming that wave functions go to zero at the oxide-semiconductor inter-

face. This assumption is equivalent to assuming an infinite potential barrier at the interface. It is considered to be justified since the barrier height at the interface is high enough (~ 3.1 eV) and hence, the contribution of the wave function tail inside the oxide is extremely small. Moglestue [5] extended the self-consistent calculations to hole inversion charges in the same way as Stern did, but used the Fermi-Dirac Statistics.

Using the self-consistent results, Ohkura [6] reported the dependence of self-consistent solution on the substrate doping concentration. He showed that increase in doping level results in shifting of subthreshold curves, especially for impurity concentration greater than 10^{17} cm^{-3} . He also proposed a method for transferring the QM effects into the semi-classical calculation through the modification of gate oxide thickness and flat band voltage.

Since the quantization of electrons in inversion layer modifies the electron density, the dependence of surface potential at the interface on the gate voltage must be calculated considering the QM effects [7]. Actually it is found that, due to this dependence both the non-degenerate and degenerate approximations have deviated increasingly from the actual quantum case with increasing gate voltage. This deviation also increases with decreasing oxide thickness.

The inversion layer capacitance (C_{inv}), inherent to MOS structure, plays a significant role in ultra-thin gate oxide capacitance. The total gate capacitance (C_{tot}) is the series combination of the oxide capacitance (C_{OX}) and C_{inv} . With the increased demand of scaling of MOS, gate oxide becomes thinner resulting in larger C_{OX} and thereby causing larger reduction of C_{tot} and also of the transconductance due to C_{inv} . There are two physical origins of C_{inv} : one due to finite effective density-of-states called classical inversion capacitance, C_{inv}^{DOS} and other due to the finite inversion layer thickness called QM inversion capacitance, $C_{inv}^{thickness}$. In Ref. [8], the surface carrier concentration, N_s and temperature de-

pendence of C_{inv} is qualitatively expressed as the series capacitance of these two capacitances. It is shown that, at lower N_s , C_{inv} is determined by the first one while at higher N_s , C_{inv} is determined by the later origin.

In his paper, Saha [9] investigated the effects of inversion layer quantization on the performance of NMOS devices fabricated with different shapes of channel doping profiles. He showed that for nano-MOSFET devices, suitable channel profile engineering could optimize the impact of QM effects and the variation in the device performance due to dopant fluctuations. Applying the self-consistent results with highly non uniform doping profiles, the dependence of QM effects on the channel doping profiles was also shown in Ref. [10]. In this reference it has been shown that introduction of low doped region at the device surface allows tailoring the threshold voltage according to the circuit applications while high doping leads to high threshold values for realistic applications. In addition, this region reduces the electron effective field for a given charge sheet density resulting in an improvement of electron effective mobility. Though the displacement of inversion charge from the silicon surface causes the reduction of total gate capacitance with respect to C_{OX} , no significant additional degradation has been found due to the introduction of low-doped epitaxial layer.

Previously, the effects of channel quantization on the capacitance characteristics was determined by the AC charge centroid of the charge layer, although this is not directly relevant to predict transistor current. In fact, a model of DC charge centroid can accurately explain the direct current in a transistor. The conventional method of electrical oxide thickness characterization using C-V measurements in the accumulation region reflects the approximate value of the AC centroid in the inversion region but not the DC centroid. In Ref. [11], an empirical model for the DC charge centroid in terms of the gate voltage, threshold voltage and oxide thickness was developed. This model developed a one dimensional

simulator using a self-consistent method by solving Schrödinger's and Poisson's equations iteratively along with Fermi-Dirac Statistics. Employing this model, a universal expression for this DC charge centroid from the accumulation to depletion region was later derived by Liu et.al. [12]. They considered the finite charge layer thickness due to quantization effects in all operating regions and thereby proposed an accurate model for C-V characterization.

In the modeling of carrier quantization in strong inversion and accumulation, it is commonly assumed that a semi-classical model is acceptable near flat bands, when confinement of majority carriers is weak due to small surface electric field. However, this assumption is not correct, as the carrier quantization effects extends to the weak accumulation and flat band operating regions. The presence of abrupt potential discontinuity at the Si/SiO₂ interface causes a dark space of a few nanometers, where the concentration of majority carriers is much lower than in the bulk even for a small or vanishing electric field [13]. This quantum effect is practically significant only if the dark space is comparable to or larger than the Debye screening length in the semiconductor. When screening length is much larger than the dark space, no quantization effect is observed. Again, while the Debye length depends both on the doping and the temperature, the dark space depends only on the temperature. Therefore, a significant capacitance attenuation is observed at room temperature only for relatively high doping concentration ($\geq 1 \times 10^{17} \text{ cm}^{-3}$).

Self-consistent solution by coupling Schrödinger's and Poisson's equations is very much computationally expensive. Various models [2, 14, 15, 16, 17, 18, 19] were devised to reduce the computational hazards without sacrificing the accuracy. One model proposed by Hareland et. al. [1] utilized analytical descriptions for the first three subbands of a 2-D density-of-states in a quantized electron inversion layer. This model predicted significant threshold voltage shifts and dif-

ferent oxide thicknesses compared to semi-classical simulations. Later Jallepalli et. al. [20] provided a compact analytical model to describe the threshold voltage shifts due to QM effects as a function of the doping concentration and oxide thickness. The increase of the effective oxide thickness due to quantization was presented as a function of the oxide field for a range of doping concentrations.

1.2 Scope of the Work

Various research works in the field of QM effects in MOS structures used a boundary condition in their wave function calculation that wave function penetration into the oxide is zero, as proposed by Stern [4]. The validity of this assumption lies in the fact that the barrier height at the interface of oxide-semiconductor is high and the error is negligible compared to the device dimensions. But the current trend in scaling down in the MOS feature size questions its validity as today's submicron devices progressively approach to the dimensions in which the error is no longer insignificant. This effect was first pointed out in Ref. [21] for a device of $\leq 20 \text{ \AA}$ gate oxide thickness. This Ref. showed that the conventional assumption leads to an over-estimation of the distances moved by the carriers from the interface by a few angstroms and proposed a new boundary condition called the asymptotic boundary condition that accounts this effect.

Throughout the present work, it has been studied whether there exists any justification of the use of the conventional boundary condition as proposed by Stern and its appropriateness in the ultra-thin gate oxide MOS modeling. The boundary conditions are also employed to study various physical and electrical parametric variation, such as doping density variation, oxide thickness variation and electric field variation.

Throughout the work, a two terminal MOS capacitor is considered. The interface charge is neglected. Body-effect is considered to be absent. The room

temperature is assumed for all calculations. Polysilicon effect is not considered as gate was thought to be made of a metal, Al. Moreover, the main focus was given onto the strong inversion. The inversion well at the Si/ SiO₂ interface is assumed to be exponential at strong inversion. In spite of all these approximations, the results obtained through this study can draw significant attention of device engineers. Especially for submicron devices, the significance becomes prominent.

1.3 Organization of the Thesis

The semi-classical and quantum mechanical view of MOSFET are reviewed in chapter 2. The analytical expressions for inversion charge density, shift of DC charge centroid from the interface and the effective gate capacitance including quantum effects are presented in this chapter. The conventional method of calculating eigenenergies and wave functions is also described briefly in this chapter. The present work uses quantum mechanical generalized impedance concept analogous to transmission line [22] along with Green's function formalism [23] to calculate eigenenergies and wave functions. A brief discussion of these methods is presented in chapter 3.

Chapter 4 presents the calculated results using both boundary conditions. The results obtained by varying different parameters, such as oxide thickness, doping concentration, surface electric field and gate voltage are presented in this chapter. A comparison between the effects of both boundary conditions is made in this chapter.

The concluding remarks and suggested recommendations for future work are included in chapter 5 of this thesis.

Chapter 2

REVIEW OF MOS THEORY: SEMI-CLASSICAL AND QUANTUM APPROACH

An n-channel metal-oxide-semiconductor (NMOS) transistor is based on the idea developed more than half a century ago by J.E. Lilienfeld in the early 1930's. Now-a-days this device is getting increasingly keen attention from the scientists and and engineers due to its relatively lower cost, less power consumption and smaller real estate area than the other types of transistor devices i.e. bipolar junction transistors. A simple preview of this NMOS transistor is offered in this chapter.

2.1 Basic Structure

A simplified structure of NMOS transistor (enhancement type) is shown in Fig. 2.1. The transistor is formed on a p-type silicon wafer (doping concentration generally ranges from 10^{16} to 10^{18} cm^{-3}), called body or substrate. The dopant concentration is assumed uniform throughout the body, unless otherwise specified. An insulator, typically silicon-dioxide and hence often referred to simply as oxide and usually of 35 to 100 Å thickness, covers the central structure. The body interface to the oxide is often called as surface. On the top of this oxide is a low-resistivity electrode, called gate. Polycrystalline silicon (heavily doped p or n-type e.g. 10^{20} cm^{-3}) is commonly used for the gate. Aluminium metal is also used for the gate. On the two sides, just outside the “shadow” of the gate, are shown the n^+ regions (heavily doped n, which causes low-resistivity for these regions) formed by implanting donor atoms indicated as source and drain; these regions are typically 0.04 to 0.2 μm deep. The region between them is called the channel.

Under the condition when sufficiently positive gate-source voltage (V_{GS}) is applied, positive charges are placed on the gate which repel the holes from the surface, thus leaving the latter depleted. The resulting depletion region contains a number of negatively charged acceptor ions; this situation is called as depletion.

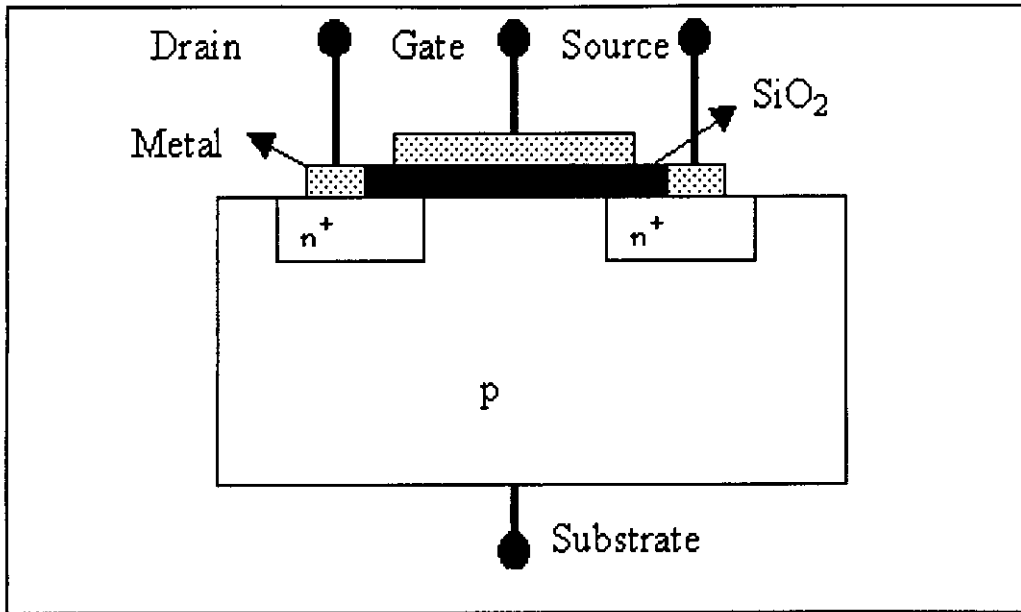


Figure 2.1: An enhancement type n-channel MOS transistor.

By applying more and more positive V_{GS} , the surface even can be made attractive to electrons. In this situation, the surface of the p-type body, which normally would have an abundance of holes, now has plenty of electrons; the situation is termed as inversion and the layer of electrons at the surface is called as inversion layer.

The electron-density in the channel can be varied through the gate potential. This can cause a variation of “strength” of the connection between the two n^+ regions, resulting in transistor action. If the two n^+ regions are biased at different potentials, the lower potential one acts as a source for electrons and the higher potential one as the drain. Electrons flow from the source through the channel and collected by the drain. The source, drain, gate and body are denoted by S , D , G and B respectively.

2.2 Energy Band Diagram

2.2.1 Zero Bias

The energy band diagrams of two ideal MOS structures [24], one with p-type substrate and the other with n-type substrate at equilibrium condition for zero bias are shown in Figs. 2.2 and 2.3, respectively. In these figures, Φ_m is the work function for the metal-SiO₂ interface which is the energy required to move an electron from metal Fermi level to SiO₂ conduction band; Φ_{si} is the work function for Si-SiO₂ interface which is the energy required to move an electron from Si-Fermi level to SiO₂ conduction band; χ is the semiconductor electron affinity and is measured from semiconductor conduction band to SiO₂ conduction band; E_g is the energy gap for semiconductor and is the energy difference between semiconductor conduction band and semiconductor valence band; ϕ_B , also expressed as ϕ_F is the separation between the Fermi level and intrinsic level in Si and is an indication of doping concentration in the substrate; E_i , E_C and E_V are intrinsic Fermi level, conduction band and valence band edges, respectively.

For idealized case, $\Phi_m = \Phi_{si}$. But for an actual device, this condition does not hold as metal Fermi level is at lower level than the semiconductor Fermi level. As a result, a tilting is found for oxide conduction band and E_C bends near the surface. Under such conditions, the difference between the two work functions can be written as [25]

$$\Phi_{ms} = \Phi_m - \Phi_{si} = \Phi_m - \left(\frac{\chi}{q} + \frac{E_g}{2q} + \phi_F \right), \quad \text{for p-type substrate} \quad (2.1)$$

$$\Phi_{ms} = \Phi_m - \Phi_{si} = \Phi_m - \left(\frac{\chi}{q} + \frac{E_g}{2q} - \phi_F \right), \quad \text{for n-type substrate} \quad (2.2)$$

2.2.2 Positive Bias

For an enhancement type NMOS device with a small positive gate voltage V , the metal potential increases and thereby lowers the metal Fermi level by an amount

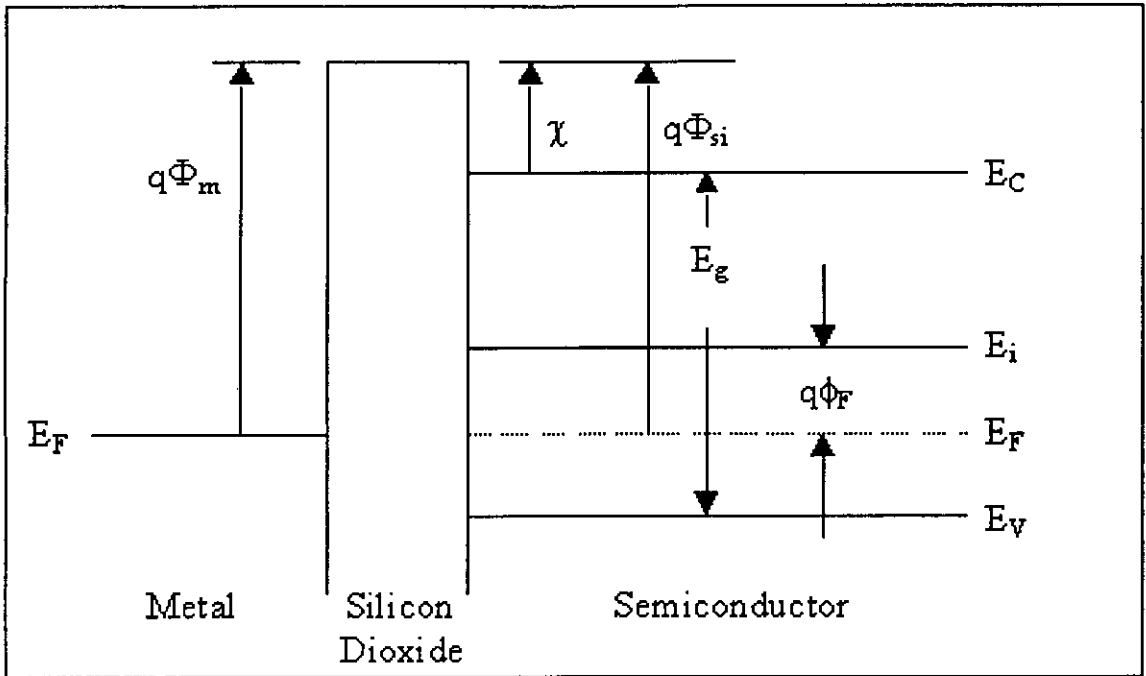


Figure 2.2: Energy band diagram for zero bias condition assuming $\Phi_m = \Phi_{si}$ for p-type substrate.

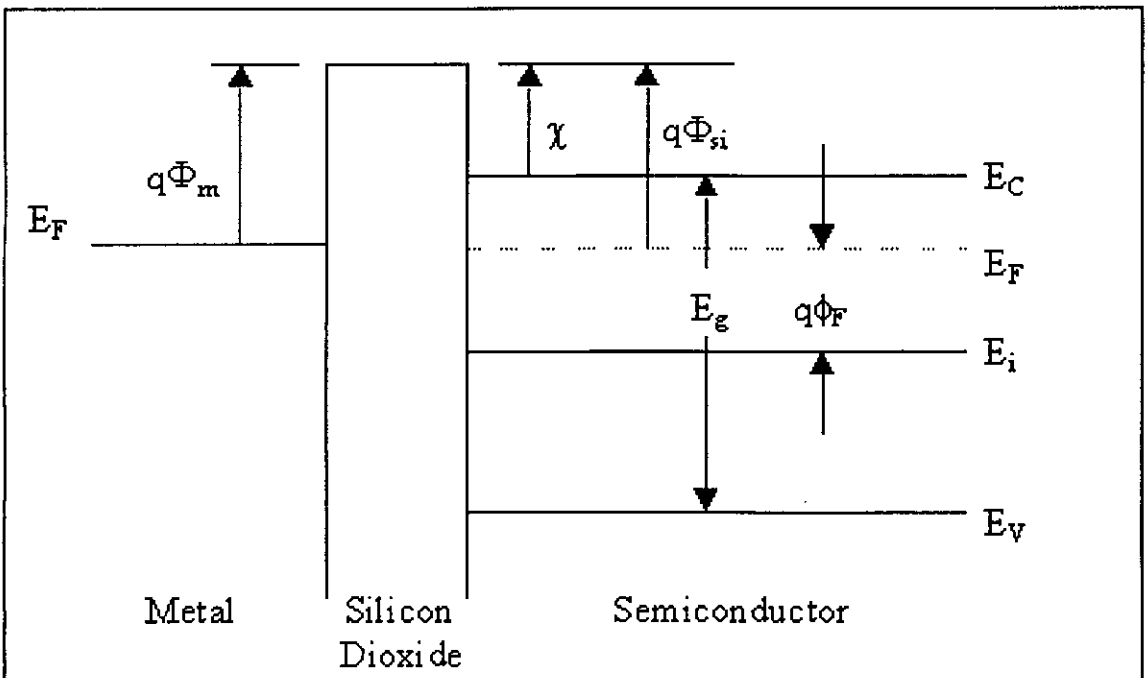


Figure 2.3: Energy band diagram for zero bias condition assuming $\Phi_m = \Phi_{si}$ for n-type substrate.

equal to qV relative to its equilibrium condition as shown in Fig. 2.4. The electron and hole concentrations in the bulk are given by

$$n_{po} = n_i e^{\frac{E_F - E_i}{kT}} \quad (2.3)$$

$$p_{po} = n_i e^{\frac{E_i - E_F}{kT}} \quad (2.4)$$

under the assumptions that

$$e^{\frac{E_C - E_F}{kT}} \gg 1 \quad \text{and} \quad (2.5)$$

$$e^{\frac{E_V - E_F}{kT}} \ll 1 \quad (2.6)$$

where n_i is the intrinsic electron concentration (for Si, it is equal to $1.5 \times 10^{16} \text{ cm}^{-3}$), k is Boltzman's constant and T is assumed to be equal to room temperature i.e. $T = 300^0 \text{ K}$.

With positive voltage applied to the gate, a depletion region for holes is created near the interface, as then positive charges are deposited on the metal and hence, repel holes from the regions near the interface. As a result, E_i moves closer to E_F near the interface as required by Eq. 2.4, which causes band bending near the interface as shown in Fig. 2.4.

If positive gate voltage is continued to increase, the bands bend more strongly. At a certain level of gate voltage, E_i crosses E_F [Fig. 2.5]. From equation 2.3, this results in a large electron concentration near the interface. In this case, the p-type semiconductor is converted to n-type near the surface. This situation is inversion. Fig. 2.5 shows the condition under strong inversion. In this figure, ϕ defines a potential to give the extent of band bending of E_i from its equilibrium condition.

Electron and hole concentrations in terms of band bending potential ϕ (Fig 2.5), can be expressed as

$$n_p = n_{po} e^{\frac{q\phi}{kT}} \quad (2.7)$$

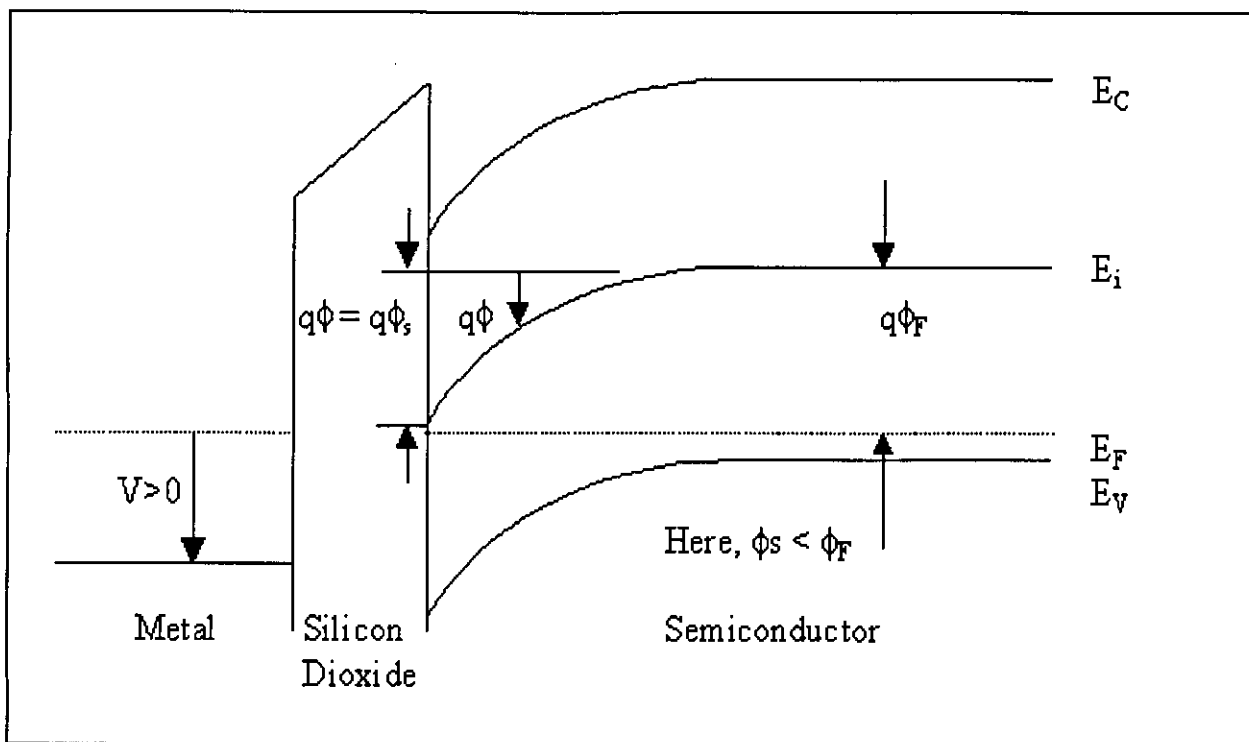


Figure 2.4: Energy band diagram under depletion condition.

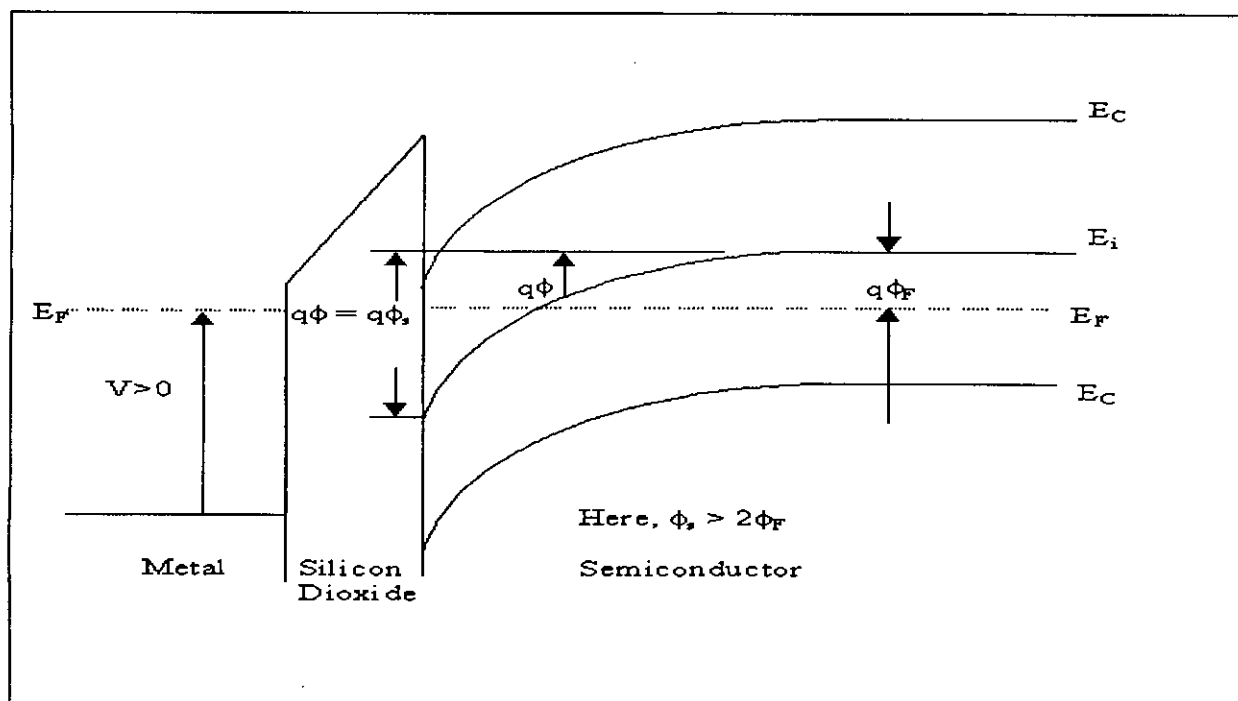


Figure 2.5: Energy band diagram under strong inversion condition.

$$p_p = p_{po} e^{-\frac{q\phi}{kT}} \quad (2.8)$$

where, ϕ is considered to be positive when bands bend downward. At the Si-SiO₂ interface $\phi = \phi_s$, where ϕ_s is called the surface potential.

2.3 Semi-classical Approach

At zero bias, the band bending at the semiconductor layer is determined by the difference of the work functions of the metal and the semiconductor. This band bending may be compensated by applying a voltage difference, called *Flat-Band Voltage*, V_{FB} is given by [24]

$$V_{FB} = \Phi_{ms} - \frac{Q_i}{C_{OX}} \quad (2.9)$$

where, Φ_{ms} is defined in Eqs. 2.1 and 2.2. For Al-Si work function potential difference, Φ_{ms} is always negative and is most negative for heavily doped p-type Si, because for aluminium gate, Φ_m is constant and is equal to 0.6 V, while Φ_s is negative and depends on the doping concentration of the semiconductor [24, 26].

In Eq. 2.9, Q_i is the interface charge and C_{OX} is the oxide capacitance per unit area, given as

$$C_{OX} = \frac{\epsilon_{OX}\epsilon_0}{T_{OX}} \quad (2.10)$$

where, ϵ_{OX} is the relative permittivity of the oxide, ϵ_0 is the absolute permittivity and T_{OX} is the oxide thickness. For simplicity, Q_i is assumed to be zero and hence, Eq. 2.9 reduces to

$$V_{FB} = \Phi_{ms} \quad (2.11)$$

If the voltage applied to the gate is negative, the band bends such that the Fermi level at the interface is closer to the top of the valence band than in the bulk. Hence, the majority carrier concentration at the interface is larger than that in the bulk [27]. This situation is termed as accumulation. Therefore,

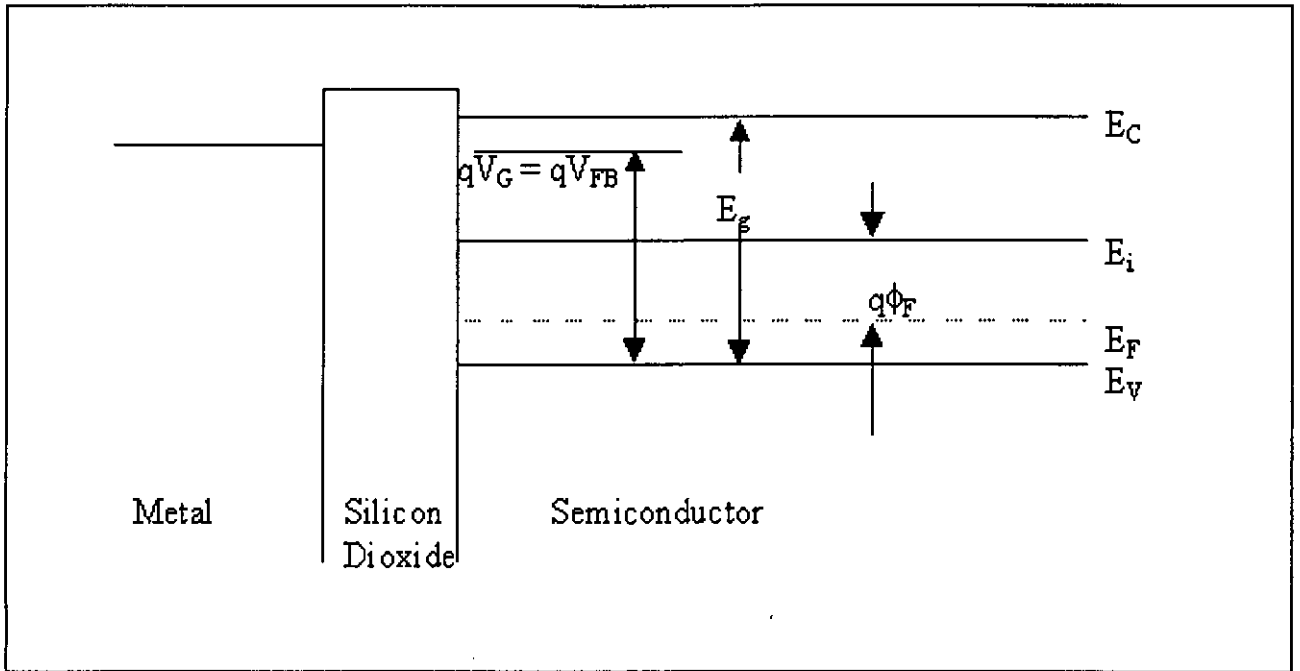


Figure 2.6: Energy band diagram at flat band condition ($\Phi_{ms} \neq 0$).

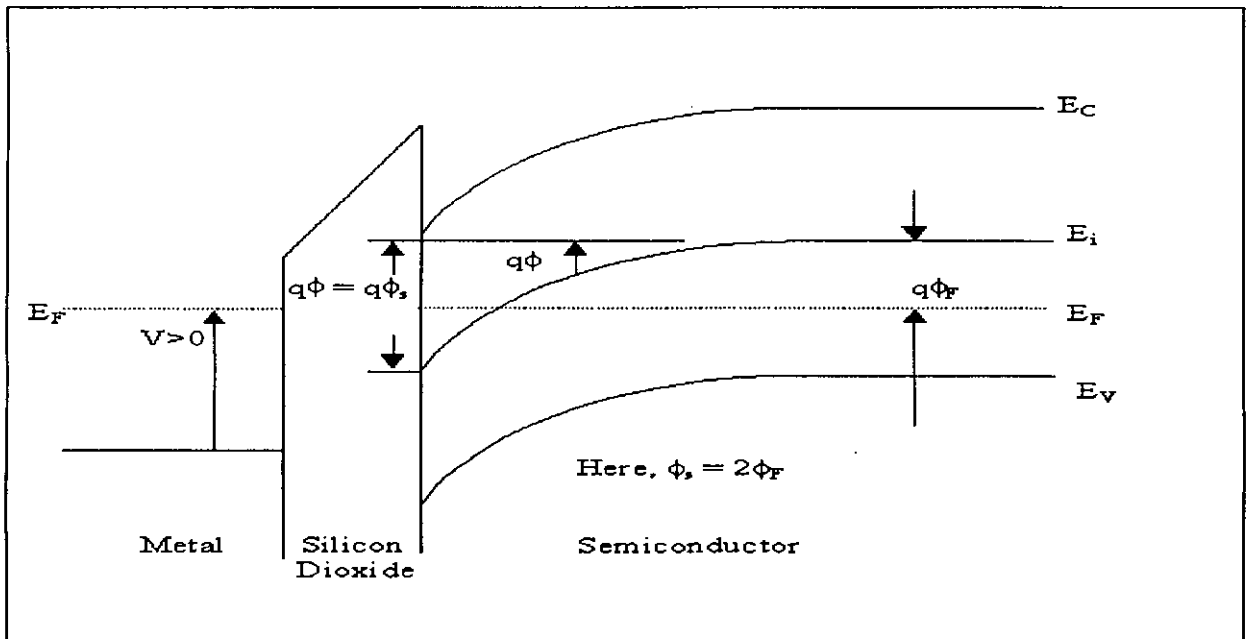


Figure 2.7: Energy band diagram at onset of strong inversion condition.

there exists four situations depending on the voltage level applied to the gate. Mathematically, all four situations can be expressed as follows [26]:

Flat-Band Condition

$$V_{GB} = V_{FB} \quad (2.12)$$

$$\phi_s = 0 \quad (2.13)$$

Accumulation Condition

$$V_{GB} < V_{FB} \quad (2.14)$$

$$\phi_s < 0 \quad (2.15)$$

Depletion Condition

$$V_{GB} > V_{FB} \quad (2.16)$$

$$0 < \phi_s < \phi_F \quad (2.17)$$

Inversion Condition

$$V_{GB} > V_{FB} \quad (2.18)$$

$$\phi_s \geq \phi_F \quad (2.19)$$

V_{GB} is the applied potential between gate and substrate and ϕ_s is the surface potential. Depending on the value of ϕ_s , the inversion region is roughly divided into two regions: weak and strong inversion. The weak inversion is defined as:

$$\phi_F \leq \phi_s < 2\phi_F \quad (2.20)$$

From Fig. 2.7, the onset of strong inversion is defined as [24, 26]:

$$\phi_s = 2\phi_F \quad (2.21)$$

and in strong inversion,

$$\phi_s \geq 2\phi_F \quad (2.22)$$

Of all these, strong inversion is the most important operating region. The voltage required for the onset of the strong inversion is called as threshold voltage, V_T which can be expressed as [26]:

$$V_T = V_{FB} + 2\phi_F + \gamma\sqrt{2\phi_F} \quad (2.23)$$

where,

$$\gamma = \frac{\sqrt{2q\epsilon_{si}\epsilon_0 N_A}}{C_{OX}} \quad (2.24)$$

and is called the body effect coefficient; here, N_A is the acceptor doping concentration and ϵ_{si} is the relative permittivity of the semiconductor. According to the *charge sheet approximation*, the potential drop across the inversion layer is negligible and hence, all of the surface potential drop occurs across the depletion region of the p-type substrate. The validity of this approximation lies in the fact that most of the charge in the inversion layer is concentrated so close to the surface that this layer is considered to be a sheet of negligible thickness compared to the depth of the depletion region and the depletion region is implied to be devoid of electrons. Moreover, using the *depletion approximation*, it is further assumed that the mobile carrier concentration, p is negligible in comparison to the acceptor concentration inside the depletion region. Under these assumptions, Poisson's equation, given by

$$\frac{d^2\phi}{dz^2} = \frac{-q[p - n - N_A]}{\epsilon_{si}\epsilon_0} \quad (2.25)$$

reduces to

$$\frac{d^2\phi}{dz^2} = \frac{-qN_A}{\epsilon_{si}\epsilon_0} \quad (2.26)$$

The solution of the Eq. 2.26 then gives the depletion depth, z_d ,

$$z_d = \sqrt{\frac{2\epsilon_{si}\epsilon_0}{qN_A}\phi_s} \quad (2.27)$$

From Eq. 2.27, it is obvious that z_d is the function of ϕ_s . At threshold, z_d reaches its maximum value and after that it will not be increased with the increase of ϕ_s . Hence, in strong inversion, z_d is given by [24, 26],

$$z_d = 2\sqrt{\frac{\epsilon_{si}\epsilon_0}{qN_A}\phi_F} \quad (2.28)$$

The gate voltage is usually expressed as [26],

$$V_G = V_{FB} + \phi_s - \frac{Q_B + Q_I}{C_{OX}} \quad (2.29)$$

where, Q_I is the inversion layer charge per unit area, Q_B is the charge per unit area due to ionized acceptor impurities in the depletion region, given by

$$Q_B = -qz_dN_A \quad (2.30)$$

and ϕ_s is greater than $2\phi_F$. In semi-classical approach, to calculate Q_I , first the depletion region charge, Q_B is calculated, using Eqs. 2.28 and 2.30. Next the total charge in the semiconductor under the oxide per unit area, Q_C , which is the sum of inversion layer and depletion region charges, is calculated and then Q_B is deducted from Q_C . Here [26],

$$Q_C = -\sqrt{2q\epsilon_{si}\epsilon_0N_A}\sqrt{\phi_s + \phi_t e^{\frac{\phi_s - 2\phi_F}{\phi_t}}} \quad (2.31)$$

where, $\phi_t = \frac{KT}{q}$. The gate capacitance at inversion can be expressed as a series combination of oxide capacitance, C_{OX} , depletion capacitance, C_B and the inversion capacitance, C_I [26], where,

$$C_B = -\frac{dQ_B}{d\phi_s} \quad (2.32)$$

$$C_I = -\frac{dQ_I}{d\phi_s} \quad (2.33)$$

2.4 Quantum Mechanical Approach

2.4.1 Basic Formulation

As already discussed in the previous chapter that at high doping concentrations (10^{17} to 10^{18} cm^{-3}) QM effects are nontrivial for device engineers. At this level of doping concentration, quantization results in a redistribution of the carrier density near the Si/SiO₂ interface as compared to the semi-classical prediction. Hence, a QM calculation is necessary to accurately describe the behaviour of the electron inversion layer. One common approach to make QM calculation is to solve coupled Schrödinger's and Poisson's equations in a self-consistent manner. A number of assumptions are used to obtain a balance between acceptable physical accuracy and computational efficiency when analyzing the electrical behaviour of MOS [4]:

1. Effective mass approximation is valid. This approximation leads to decouple the 3-D Schrödinger's equation into a 1-D Schrödinger's equation that describes the envelope function normal to the interface.
2. The envelope wave function vanishes at the oxide-semiconductor interface as the potential barrier ($\sim 3.1 \text{ eV}$) to electrons in the well is assumed as infinitely high at the Si/SiO₂ interface.
3. Surface states are neglected and an equivalent electric field replaces the effect of any changes in the oxide or insulator adjacent to the semiconductor.

In QM consideration, the band bending can be characterized by an electrostatic potential, $\phi(z)$. The electronic wave function parallel to the interface is assumed to be a plane wave and as effective mass approximation is considered, the wave function is expressed as the product of Bloch function at the bottom

of the conduction band and an envelope function normal to the interface (z -direction) [4], i.e.,

$$\zeta_{ij}(x, y, z) = \psi_{ij}(z)e^{i\theta\pi}e^{i\kappa_1x+i\kappa_2y} \quad (2.34)$$

where κ_1 and κ_2 are measured relative to the band edge, θ depends on κ_1 and κ_2 , $\psi_{ij}(z)$ is the solution of

$$\frac{d^2\psi_{ij}}{dz^2} + \frac{2m_{zi}}{\hbar^2}[E_{ij} + q\phi(z)]\psi_{ij}(z) = 0 \quad (2.35)$$

where m_{zi} is the effective mass perpendicular to the interface in the i th valley, E_{ij} and ψ_{ij} are the eigenenergy and normalized eigen function (the envelope function) respectively, of the j th subband in the i th valley. Here, parabolic bandstructure is used.

According to the conventional approach, for calculating the bound solutions of Eq. 2.35, two boundary conditions are used [4]:

$$\psi_{ij}(\infty) = 0 \quad (2.36)$$

$$\psi_{ij}(0) = 0 \quad (2.37)$$

where, $z = \infty$ and $z = 0$ are the bulk and the interface, respectively. Each eigenvalue, E_{ij} found from the solutions of Eq. 2.35 is the bottom of a continuum of levels called a subband. The potential $\phi(z)$ is the solution of Poisson's equation [4]:

$$\frac{d^2\phi}{dz^2} = -\frac{\rho_{depl}(z) + \rho_{inv}(z)}{\epsilon_{si}\epsilon_0} \quad (2.38)$$

Unlike the semi-classical calculation, inversion electron density, ρ_{inv} is given as follows

$$\rho_{inv}(z) = -q \sum_{ij} n_{ij} |\psi_{ij}(z)|^2 \quad (2.39)$$

where n_{ij} is the carrier concentration in the j th subband of the i th valley, given by [4]

$$n_{ij}(E_{ij}) = \frac{n_{vi}m_{di}KT}{\pi\hbar^2} \times \ln\left(1 + e^{\frac{E_F - E_{ij}}{KT}}\right) \quad (2.40)$$

n_{vi} is the valley degeneracy (which are degenerate in pairs in the effective mass approximation), m_{di} is density-of-states effective mass per valley. $\rho_{depl}(z)$ is the depletion layer charge density, expressed as [4]

$$\rho_{depl}(z) = \begin{cases} -qN_A & \text{if } 0 < z < z_d \\ 0 & z > z_d \end{cases} \quad (2.41)$$

The boundary conditions for Eq. 2.38 are that $\frac{d\phi}{dz}$ vanishes for large z i.e. in the bulk and that its value at the surface equals $-F_s$, given by [4]

$$F_s = \frac{q(N_{inv} + N_{depl})}{\epsilon_{si}\epsilon_0} \quad (2.42)$$

where, F_s is the surface electric field and N_{inv} and N_{depl} are the number of charges per unit area in the inversion layer and in the depletion layer, respectively and expressed as

$$N_{inv} = \sum_{ij} n_{ij}(E_{ij}) \quad (2.43)$$

$$N_{depl} = z_d N_A \quad (2.44)$$

As quantization is in effect, the carriers move some distance away from the interface. So charges are now confined within a distance not equal to the physical oxide thickness, but with a larger thickness. That is, due to this QM effect, the effective electrical oxide thickness is no longer equal to the physical oxide thickness; instead, a correction factor is added to it. This factor is called DC charge centroid shift, X_{DC} . This can be expressed as [11]

$$X_{DC} = \frac{\int \rho_{inv}(z)zdz}{\int \rho_{inv}(z)dz} \quad (2.45)$$

This factor is added after multiplying with a factor $\frac{\epsilon_{OX}}{\epsilon_{si}}$ to T_{OX} to determine the effective oxide thickness. Since, the multiplying factor=1/3 ($\epsilon_{OX} = 3.9$, $\epsilon_{si} = 11.7$), the effective oxide thickness is expressed as

$$T_{EFF} = T_{OX} + \frac{1}{3}X_{DC} \quad (2.46)$$

The effective oxide capacitance can be expressed by

$$C_{EFF} = \frac{\epsilon_{ox}\epsilon_0}{T_{EFF}} \quad (2.47)$$

The expression for threshold voltage are similar to Eq. 2.23 and can also be expressed in the form

$$V_T = V_{FB} + 2\phi_F + \frac{qN_{depl}}{C_{OX}} \quad (2.48)$$

The gate voltage can be expressed by Eq. 2.29, with Q_I given by

$$Q_I = -qN_{inv} \quad (2.49)$$

and Q_B given by Eq.2.30. Hence,

$$V_G = V_{FB} + \phi_s + \frac{q(N_{depl} + N_{inv})}{C_{OX}} \quad (2.50)$$

C_{OX} is replaced by C_{EFF} expressed by Eq. 2.47 instead of Eq. 2.10 to account the QM effect. The new expression for ϕ_s used in Eq. 2.50 is given as [11]

$$\phi_s = 2\phi_F - \frac{X_{DC}Q_I}{\epsilon_{si}\epsilon_0} \quad (2.51)$$

2.4.2 Approximate Techniques of QM Solution

Since the self-consistent formulation, outlined in the previous section, is complicated to implement and computationally time-consuming, a number of approximate techniques have been proposed to obtain QM solutions.

2.4.2.1 Airy Function Approximation

The simplest approximation is to replace $\phi(z)$ in Eq. 2.35 by $-F_s z$ for $z > 0$ and by an infinite potential barrier for $z < 0$. This is sometimes called the triangular-potential approximation [4].

Using the triangular-potential, the general solution of Eq. 2.35 is a combination of the two Airy functions $\text{Ai}(z')$ and $\text{Bi}(z')$ [5]

$$\psi_{ij} = \alpha \text{Ai}(z') + \beta \text{Bi}(z') \quad (2.52)$$

with

$$z' = (2m^* q F_s \hbar^{-2})^{1/3} [z - \frac{E_{ij}}{q F_s}] \quad (2.53)$$

where α and β are constants. As $\text{Bi}(z')$ diverges for $z \rightarrow \infty$, this is rejected as a solution. $\text{Ai}(z')$ decays monotonically to zero for $z' > 0$ and oscillates for $z' < 0$. E_{ij} is chosen such that $\text{Ai}(z')$ has j roots and ψ_{ij} is taken to be zero for z' below this j th root. Then the energy becomes [5]

$$E_{ij} = (\frac{\hbar^2}{2m^*})^{1/3} [\frac{3}{2} \pi q F_s (j - \frac{1}{4})]^{2/3} \quad (2.54)$$

2.4.2.2 Variational Approach

The triangular-approximation described in the previous subsection fails when charge density per unit area in the inversion layer is comparable to or exceeds that in the depletion layer. In the electric quantum limit (i.e. when only one subband is occupied), the variational approach is a reasonable estimation for the energy of the lowest subband. For this, Fang and Howard introduced a wavefunction of the lowest subband [4].

$$\psi_{10}(z) = \frac{b^{3/2}}{\sqrt{2}} z e^{-bz/2} \quad (2.55)$$

where the parameter b is determined by minimizing the energy of the system using the wavefunction given by Eq. 2.55. From the variational approach, the

approximate expression for the ground state of the subband energy, E_{10} can be found as [4]

$$E_{10} = 2 \left(\frac{q^2 \hbar}{\sqrt{m_{zi} \epsilon_{si}}} \right)^{2/3} \left(N_{depl} + \frac{55}{96} N_{inv} \right) \left(N_{depl} + \frac{11}{32} N_{inv} \right) \quad (2.56)$$

Eigenenergies for the higher lying subbands are calculated (following Stern [4]) using a perturbation technique

$$E_{ij} = E_{ij,depl} - \frac{q^2 F_{depl} F_{inv} z_0^2}{4 E_{ij,depl}} - \frac{4 E_{ij,depl}}{15 q F_{depl} z_{depl}} + q F_{inv} z_0 - 10 \text{meV} \quad (2.57)$$

where $E_{ij,depl}$ is the energy obtained from Eq. 2.54 using only the surface electric field, F_s , due to the depletion charges. z_0 is the average distance of the charge density away from the interface associated with the variational wave function, and F_{depl} and F_{inv} are the surface electric fields due to the depletion and inversion layer charges, respectively. However, in order to obtain better overall agreement with self-consistent calculations, a correction factor of approximately -10 meV was added to the eigenenergies calculated in Eq. 2.57.

Chapter 3

TRANSMISSION LINE ANALOGY AND GREEN'S FUNCTION FORMALISM: AN OVERVIEW

After Stern's publication [4] it is evident that QM effects can no longer be neglected to make a balance between the theoretical model and the practical results with the increasing trend of scaling down the MOS feature size. To accurately model the QM effects, it is a must to solve Schrödinger's equation. But this generally requires lengthy matrix manipulation. Hence, some assumptions are made to reduce the complicity of the problem. Various researchers worked on to derive a simple solver to reduce the computational hazards in solving the QM approach. Of those, some are mentioned in chapter 1. In this chapter, a quite simple approach is presented. This approach first uses the well-known transmission line concept used in microwave engineering. Realizing the power of this approach to solve QM problems, later Green's function is introduced to calculate eigenenergies and wave functions. When these are known, other quantities of interest can be calculated easily.

3.1 Transmission Line Analogy

Transmission line analogy to solve Schrödinger's equation is described briefly as follows [22]. The well known equations for voltage (V) and current (I) used in transmission line theory are, with time variation assumed as $e^{-i\omega t}$ instead of usual $e^{i\omega t}$,

$$I(z) = I^+(e^{\gamma_r z} - \Gamma_t e^{-\gamma_r z}) \quad (3.1)$$

$$V(z) = I^+ Z_0 (e^{\gamma_r z} + \Gamma_t e^{-\gamma_r z}) \quad (3.2)$$

where, γ_r is the propagation constant and Γ_t is the wave amplitude reflection coefficient given by

$$\Gamma_t = \frac{Z_{lt} - Z_{ot}}{Z_{lt} + Z_{ot}} \quad (3.3)$$

where Z_{lt} and Z_{ot} are the load and the characteristics impedance of the transmission line, respectively.

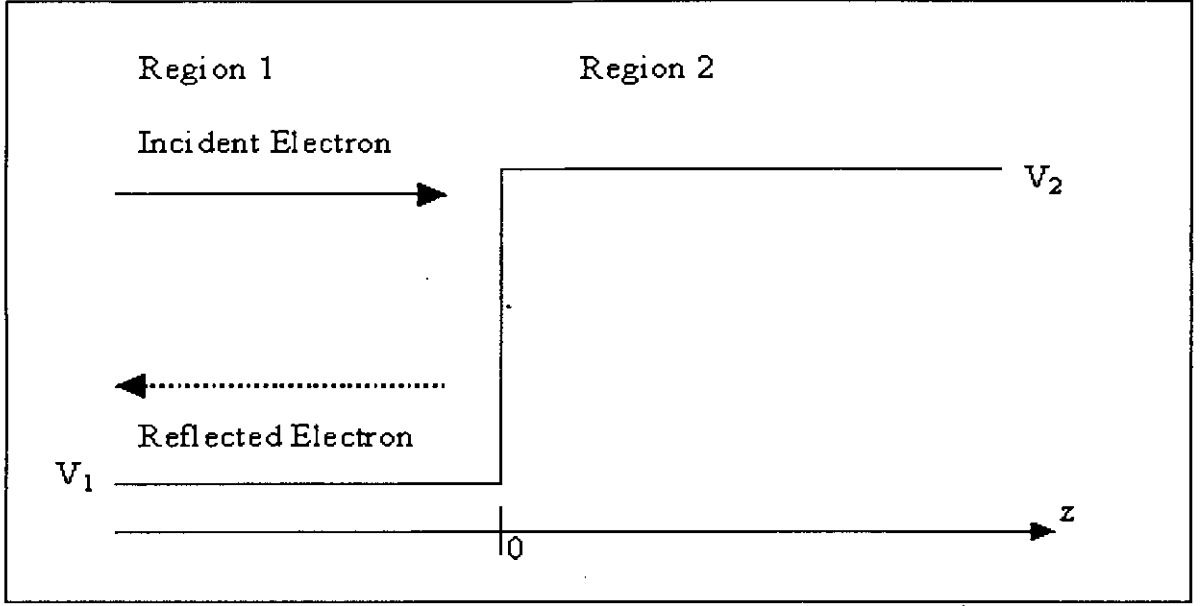


Figure 3.1: A potential barrier with an incident electron (solid line) and the reflected wave (dashed line).

If an electron with an energy E is incident on the potential barrier (Fig. 3.1), then the corresponding wave function can be expressed as

$$\psi(z) = A^+(e^{\gamma z} - \rho e^{-\gamma z}) \quad (3.4)$$

where time-variation is implicitly assumed as $e^{-\frac{iEt}{\hbar}}$ and

$$\gamma = \alpha + i\beta = i\sqrt{\frac{2m^*}{\hbar^2}(E - V)} \quad (3.5)$$

is the propagation constant, m^* is the effective mass, V is the potential and $-\rho$ is the wave amplitude reflection coefficient. For the two regions shown in Fig. 3.1, Eq. 3.4 is rewritten as

$$\psi_1(z) = A_1^+(e^{\gamma_1 z} - \rho e^{-\gamma_1 z}) \quad z < 0 \quad (3.6)$$

$$\psi_2(z) = A_2^+ e^{\gamma_2 z} \quad z > 0 \quad (3.7)$$

where, $\gamma_j = \alpha_j + i\beta_j = i\sqrt{\frac{2m_j^*}{\hbar^2}(E - V_j)}$, m_j^* and V_j ($j = 1, 2$), are the effective mass and the potential, respectively, for the j th region. Since, for $z > 0$ the

region is of infinite extent, it is evident that there is no reflection. The boundary conditions for this problem, with regard to the continuity of wave function, are

$$\psi_1(0) = \psi_2(0) \quad (3.8)$$

$$\frac{\psi'_1(0)}{m_1^*} = \frac{\psi'_2(0)}{m_2^*} \quad (3.9)$$

Using these boundary conditions an expression for ρ is found as

$$\rho = \frac{\frac{\gamma_2}{m_2^*} - \frac{\gamma_1}{m_1^*}}{\frac{\gamma_2}{m_2^*} + \frac{\gamma_1}{m_1^*}} \quad (3.10)$$

If a function, $\phi(z)$, is defined as

$$\phi(z) = \frac{2\hbar}{im^*} \frac{d\psi}{dz} \quad (3.11)$$

then,

$$\phi(z) = A^+ Z_0 (e^{\gamma z} + \rho e^{-\gamma z}) \quad (3.12)$$

where,

$$Z_0 = \frac{2\gamma\hbar}{im^*} \quad (3.13)$$

Using the value of Z_0 in Eq. 3.10, it is found that

$$\rho = \frac{Z_{0,2} - Z_{0,1}}{Z_{0,2} + Z_{0,1}} \quad (3.14)$$

where $Z_{0,1}$ and $Z_{0,2}$ are defined for region 1 and region 2, respectively.

From the above discussion, an analogy is found between voltage and current expressed by Eqs. 3.1 and 3.2 with ϕ and ψ expressed by Eqs. 3.12 and 3.4, respectively. Since, the transmission line impedance is the ratio of V and I, so the ratio of ϕ and ψ is called as wave impedance by using this analogy. This fact can be verified by using another analogy found between the equation of wave amplitude reflection coefficient for electron wave (ρ) and the equation of wave amplitude reflection coefficient for transmission line (Γ_t), as seen in Eqs 3.14 and 3.3, with Z_{lt} replaced by $Z_{0,2}$ and Z_{ot} replaced by $Z_{0,1}$. Moreover, ψ and

ϕ are continuous across the boundary between the two regions, which directly corresponds to the continuity conditions for voltage and current at the junction between two transmission lines. All these leads to a conclusion that a quantum mechanical wave impedance concept can be introduced analogous to transmission line impedance as given by at any plane z

$$Z(z) = \frac{\phi(z)}{\psi(z)} \quad (3.15)$$

Thus, transmission line concept can be applied for QM calculations. For example, the input impedance, Z_i at $z = -l$ may be expressed in terms of load impedance, Z_l at $z = 0$ as in transmission line

$$Z_i = Z_0 \frac{Z_l \cosh(\gamma l) - Z_0 \sinh(\gamma l)}{Z_0 \cosh(\gamma l) - Z_l \sinh(\gamma l)} \quad (3.16)$$

An important feature of using transmission line concept in QM calculations is its ability to calculate the eigenenergy of any arbitrary potential well. Because, from Eq. 3.15, at any eigenenergy, the wave impedances looking to the right (positive direction) and to the left (negative direction), at any plane z must be equal, i.e.

$$Z_{iR} = Z_{iL} \quad (3.17)$$

3.2 Green's Function Formalism

Green's function formalism is introduced as an extension of the transmission line analogy to include the effects of energy broadening of the density-of-states due to either finite particle lifetime in a well (i.e. when particles leak out from a quantum well) or the presence of inelastic scattering processing. Although this formalism is based on a complicated Green's function approach, it allows one to calculate easily the normalized wave functions in arbitrary 1-D quantum well structures [23].

In this formalism the QM wave impedance is redefined in terms of the logarithmic derivative of the retarded Green's function, G^R as

$$Z(z, z'; E) = \frac{2\hbar}{im_z^*} \left[\frac{\partial G^R(z, z'; E)}{\partial z} / G^R(z, z'; E) \right] \quad (3.18)$$

where G^R satisfies the equation,

$$\left[E + \frac{\hbar^2}{2m_z^*} \frac{\partial^2}{\partial z^2} - V(z) + i\epsilon \right] G^R(z, z'; E) = \delta(z - z') \quad (3.19)$$

where ϵ is an infinitesimally small positive energy. The Green's function in this context is discussed in detail in Ref. [28]. Owing to the property of G^R , $Z(z, z'; E)$ has a discontinuity at $z = z'$, and one needs two boundary conditions to determine $Z(z, z'; E)$. To obtain these boundary conditions, the potential profile is assumed flat sufficiently far from $z = z'$ in both directions. If V_R is the constant potential at $z = \infty$ and if V_L is the constant potential at $z = -\infty$, the Green's function in these regions can be expressed as [23]:

$$\overline{G^R}(z \rightarrow \infty, z'; E) \sim e^{\gamma_R(z-z')} \quad (3.20)$$

$$G^R(z \rightarrow -\infty, z'; E) \sim e^{-\gamma_L(z-z')} \quad (3.21)$$

where

$$\gamma_{R(L)} = i \sqrt{\frac{2m_z^*}{\hbar^2} (E - V_{R(L)})} \quad (3.22)$$

$\gamma_{R(L)}$ is imaginary if $E > V_{R(L)}$, else this is real. From the above relationships, the boundary conditions are found as

$$Z(z \rightarrow \infty, z'; E) = Z_0(\infty) \quad (3.23)$$

$$Z(z \rightarrow -\infty, z'; E) = -Z_0(-\infty) \quad (3.24)$$

where

$$Z_0(\pm\infty) = \frac{2\hbar}{im_z^*} \gamma_{R(L)} \quad (3.25)$$

From the properties of the Green's functions it can be shown that [28]

$$Z(z, z'; E) = Z_{iR}(z; E) \quad \text{for all } z' < z \quad (3.26)$$

$$Z(z, z'; E) = Z_{iL}(z; E) \quad \text{for all } z' > z \quad (3.27)$$

It is noteworthy that Z_{iR} (Z_{iL}) does not depend on z' as long as $z > z'$ ($z < z'$). Using transmission line analogy, Z_{iR} (Z_{iL}) can be calculated. The eigenenergies of an arbitrary quantum well can be determined using following condition:

$$Z_{iR}(z; E) = Z_{iL}(z; E) \quad (3.28)$$

as from transmission line analogy, at any eigenenergy and for all values of z inside the quantum well the above equation must be satisfied. Once an eigenenergy is found, the corresponding normalized wavefunction can be calculated using the following relationship:

$$|\psi_n(z)|^2 = \frac{4\epsilon}{\hbar} \Im \left[\frac{i}{Z_{iR}(z; E_n) - Z_{iL}(z; E_n)} \right] \quad (3.29)$$

Equations 3.28 and 3.29 are used to find the eigenenergies and wavefunctions in MOS inversion layers. Note that in calculating the wavefunctions the conventional boundary conditions that the wavefunction is zero at the oxide-semiconductor interface and inside the bulk (Equations 2.36 and 2.37) are not used. Rather, the boundary conditions used (Equations 3.23 and 3.24) assume that the potential profile is flat sufficiently far from the interface in both directions. These boundary conditions, known as the asymptotic boundary conditions, are definitely physically more acceptable boundary conditions and allow one to include the exponentially decreasing tail of the wavefunction inside the oxide in the calculation.

Chapter 4

RESULTS AND DISCUSSION

In this chapter, the results of the numerical calculations are presented. The effects of variation of gate oxide thickness (T_{OX}), doping concentration (N_A), surface electric field (F_s) and gate voltage (V_G) on various physical quantities such as inversion charge density (N_{inv}), DC charge centroid shift from the oxide-semiconductor interface (X_{DC}) and effective gate capacitance (C_{EFF}) are studied. The quantities of interest are calculated using both the boundary conditions in order to determine the effects of the choice of boundary condition on simulated results.

4.1 Potential Profile

The potential profile used in the work is approximated by an exponential function. The potential well is bounded by the oxide-semiconductor interface on one side and by the bulk on the other side. The height of the potential barrier at the interface is 3.1 eV. Conventionally, this height of barrier is considered as infinity. In this work, this conventional boundary condition is simulated by considering the barrier height as very large (~ 33.1 eV). However, in calculations with the asymptotic boundary conditions, the actual height 3.1 eV of the oxide barrier is used.

Since self consistent method is not employed in this work, an empirical formula is assumed to relate the total band bending with surface electric field, which closely matches with the self-consistent results found from Ref. [29]. The relationship between these two can be expressed by the following relationship:

$$F_s = A\phi_s^5 \quad (4.1)$$

where A is a constant that depends on doping concentration. Fig. 4.1 shows this variation of surface potential against surface electric field for three doping concentrations. As the electric field increases from 0.6 MV/cm to 1.5 MV/cm,

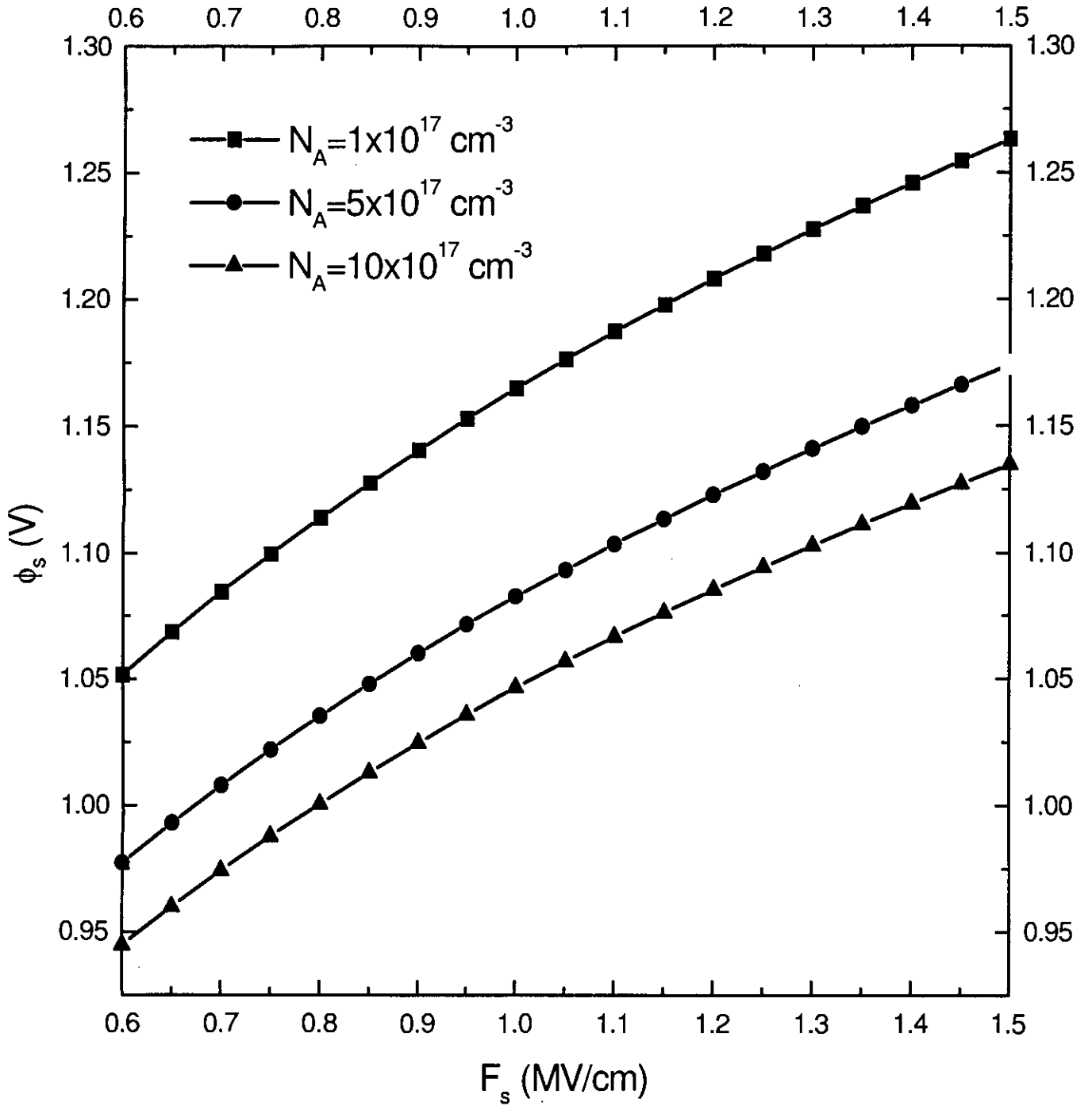


Figure 4.1: Surface Potential, ϕ_s vs. Surface Electric Field, F_s , with Doping Concentrations, $N_A = 1 \times 10^{17} \text{ cm}^{-3}$, $N_A = 5 \times 10^{17} \text{ cm}^{-3}$ and $N_A = 10 \times 10^{17} \text{ cm}^{-3}$ and oxide thickness, $T_{OX} = 20 \text{ \AA}$. Here, $T = 300^0 \text{ K}$.

the band bending increases by about 0.2 V.

Fig. 4.2 shows the potential profile for asymptotic condition under two surface electric fields i.e. $F_s = 0.75$ MV/cm and 1.5 MV/cm. The Fermi energy in Al-gate is chosen as the reference for zero energy.

4.2 General Effects of the Boundary Conditions

Eigenenergies, normalized wavefunctions and inversion charge density are calculated to study the effects of boundary conditions on these quantities.

The eigenenergies of an electron in a quantum well depends on the boundary conditions, more specifically on the degree of restriction applied to it on the boundary. If the electron wavefunction is forced to vanish on the boundaries, the eigenenergies will be higher than those found in case of an electron whose wavefunction penetrates the boundaries. This is the case in this work. Conventional assumption leads to zero wavefunction penetration at the oxide-semiconductor interface and hence the eigenenergies found using this condition are higher than the eigenenergies calculated using the asymptotic boundary condition for a given field.

Table 4.1 demonstrates the above statement. As the number of eigen state is increased, the effect becomes less pronounced, as wavefunctions for higher eigenstates penetrate more into Si and consequently are less restricted (See Fig. 4.3). In this table, the eigenenergies are calculated for two surface electric fields, $F_s = 0.75$ MV/cm and $F_s = 1.5$ MV/cm. It is found that with higher electric field, the same eigenstate is found at higher energies. When electric field is increased, the slope of the profile in the semiconductor and the amount of band bending increases. This results in a deeper and narrower quantum well i.e. increases the degree of restriction applied to the quantum well and hence, the same eigenstate occurs at a higher value.

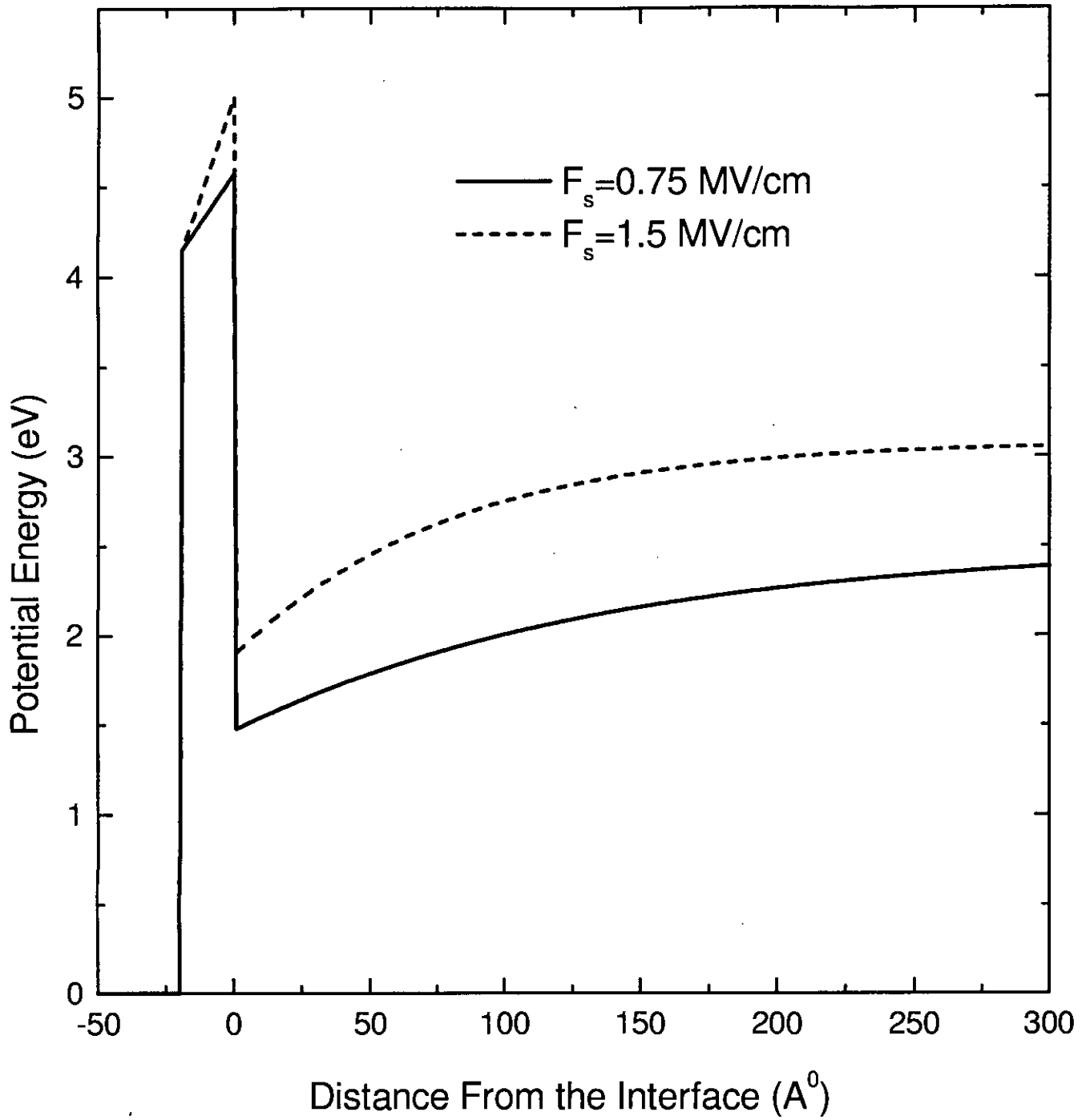


Figure 4.2: Potential profile for $F_s = 0.75$ MV/cm and 1.5 MV/cm. Doping concentration, $N_A = 5 \times 10^{17} \text{ cm}^{-3}$, Oxide thickness, $T_{OX} = 20 \text{ \AA}$, $T = 300^{\circ} \text{ K}$. The interface is at 0 \AA .

| Eigen State Number | $F_s = 0.75$ MV/cm | | $F_s = 1.5$ MV/cm | |
|-----------------------|--------------------|-------------------|-------------------|-------------------|
| | $E_{n,ASYM}$ (eV) | $E_{n,CONV}$ (eV) | $E_{n,ASYM}$ (eV) | $E_{n,CONV}$ (eV) |
| 1 | 0.6450 | 0.6551 | 1.0187 | 1.0381 |
| 2 | 0.7859 | 0.7949 | 1.2292 | 1.2458 |
| 3 | 0.8909 | 0.8991 | 1.3793 | 1.3936 |
| 4 | 0.9762 | 0.9837 | 1.4956 | 1.5080 |
| 5 | 1.0481 | 1.0549 | 1.5887 | 1.5993 |
| 6 | 1.1098 | 1.1160 | 1.6643 | 1.6734 |
| 7 | 1.1634 | 1.1691 | 1.7259 | 1.7335 |
| 8 | 1.2104 | 1.2156 | 1.7758 | 1.7821 |
| 9 | 1.2517 | 1.2564 | 1.8158 | 1.8209 |
| 10 | 1.2881 | 1.2923 | 1.8472 | 1.8512 |
| 11 | 1.3201 | 1.3238 | 1.8710 | 1.8740 |
| 12 | 1.3482 | 1.3515 | 1.8880 | 1.8900 |
| 13 | 1.3728 | 1.3758 | 1.8989 | 1.9001 |
| 14 | 1.3942 | 1.3968 | - | - |
| 15 | 1.4127 | 1.4149 | - | - |
| 16 | 1.4285 | 1.4304 | - | - |
| 17 | 1.4417 | 1.4434 | - | - |
| 18 | 1.4527 | 1.4540 | - | - |
| 19 | 1.4615 | 1.4625 | - | - |
| 20 | 1.4682 | 1.4690 | - | - |
| 21 | 1.4731 | 1.4736 | - | - |

Table 4.1: Calculated eigenenergies, E_n with respect to Si potential energy at the interface for both boundary conditions with $F_s = 0.75$ MV/cm and 1.5 MV/cm. Doping concentration, $N_A = 5 \times 10^{17} \text{ cm}^{-3}$, Oxide thickness, $T_{OX} = 20 \text{ \AA}$, $T = 300^0 \text{ K}$.

The normalized wavefunctions for three lowest eigenstates are shown in Fig. 4.3, calculated with both boundary conditions. In these figures the asymptotic wavefunction is seen closer to the interface than its conventional counterpart by about 2 \AA while the span for both boundary conditions is found same; it is also observed that the asymptotic wavefunction penetrates into the oxide region by 2-3 \AA while the conventional counterpart vanishes at the interface. Although 2 \AA is very small for general MOS devices, this can not be neglected for a device with oxide thickness of 20 \AA , since this dimension becomes comparable to the device thickness. Again, it is seen that with higher electric field, the span of wavefunction

decreases while the peak value increases, as at higher electric field quantum well is narrower and deeper. It is also seen that wavefunctions approach closer to the interface when the electric field increases.

The inversion charge density variation in the device for both the boundary conditions for two surface electric fields corresponding to the lowest three eigenenergies are shown in Fig. 4.4. Comparison of Figs. 4.3 and 4.4 shows that the inversion charge density variation is similar to the wavefunction variation i.e. for an eigenstate the asymptotic charge density plot is closer to the interface than the conventional charge density plot by about 2 \AA and at higher electric field, both asymptotic and conventional charge density plots approach closer to the interface. This similarity is consistent with Eq. 2.40, which relates inversion charge density with the normalized wavefunction, for an eigenstate. From this equation, it is also seen that the inversion charge density has an exponential dependency on the eigenenergy with respect to Si Fermi energy. Since the conventional eigenenergy is higher than the asymptotic eigenenergy with respect to the Fermi energy, the asymptotic charge density for any eigenstate is higher than the corresponding conventional one. Again, for the same reasoning, the charge densities associated with an eigenenergy, for same electric field, decrease exponentially with increasing energy and hence, the contribution of the lowest state is the most significant in the total charge density, as revealed from Figs. 4.4 and 4.6.

As surface electric field increases, the amount of band bending increases. This results in steeper and deeper quantum well and hence, eigenenergies are raised. On the other hand, as band bending increases, the Fermi energy level is also raised by the same amount, since the energy difference between the conduction band in the bulk and the Fermi energy is fixed for a fixed doping density. But, with increasing surface electric field, the rate of increase of Fermi energy level and the rate of increase of eigenenergies are not same i.e. the difference between the

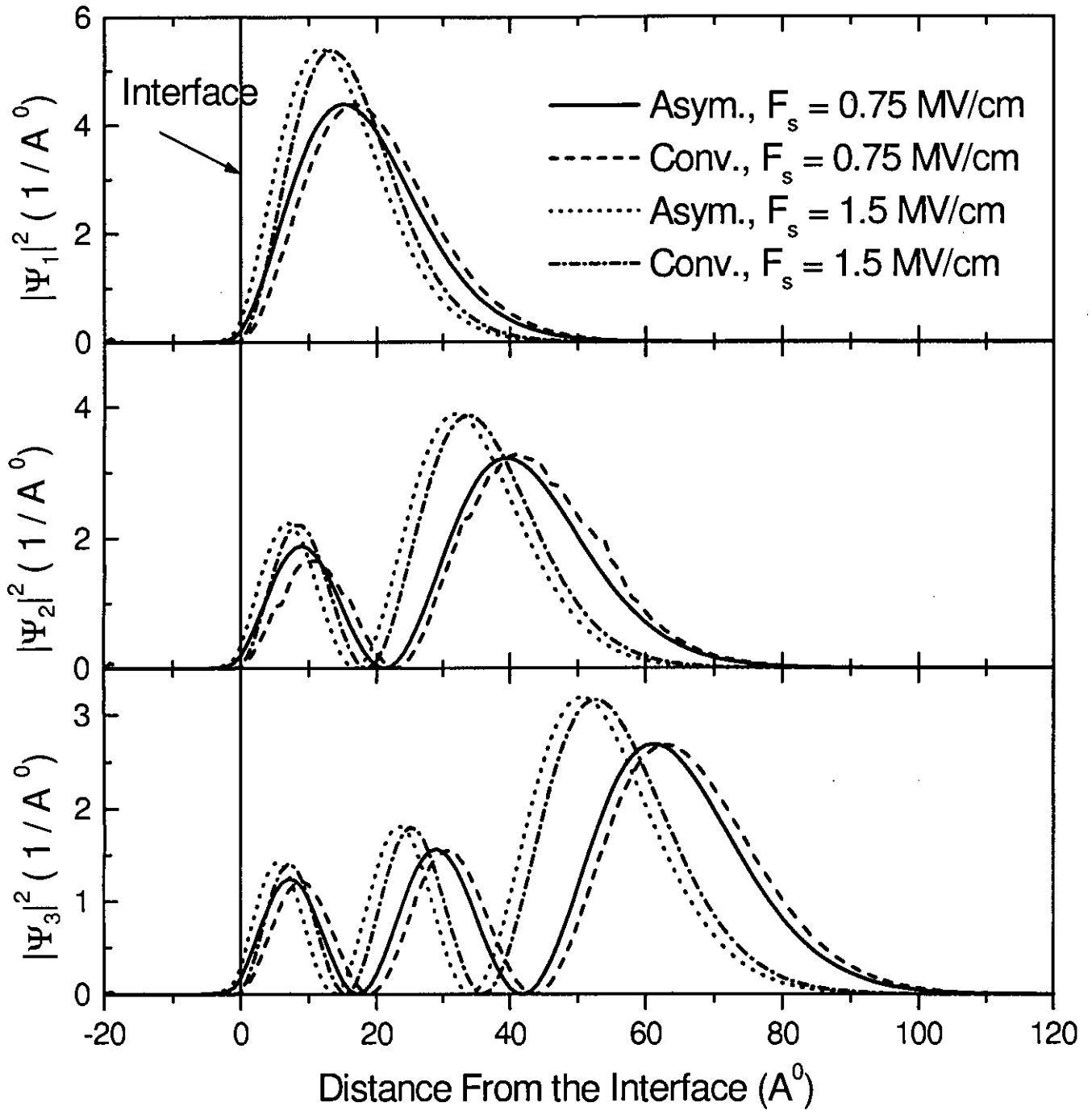


Figure 4.3: First Three Wavefunctions (normalized) for both boundary conditions with $F_s = 0.75$ and $F_s = 1.5 \text{ MV/cm}$. Doping concentration = $5 \times 10^{17} \text{ cm}^{-3}$, Oxide thickness = 20 \AA , $T = 300 \text{ K}$. The interface is at 0 \AA .

Fermi energy level and an eigenenergy ($E_F - E_i$, where i indicates an eigenstate, in Eq. 2.40) and hence, the charge density for an eigenstate are affected in a complicated way by the increasing electric field. From Fig. 4.4, it is observed that charge density for first eigenstate increases when electric field increases, while that for second and third eigenstates decreases when electric field increases. This is due to the fact that for first eigenstate, $E_F - E_i$ increases, while $E_F - E_i$ decreases for second and third eigenstate when surface electric field increases (Fig. 4.5). In other words, with increasing electric field, first eigenstate approaches closer to the Fermi energy level, but second and third eigenstates move away from the Fermi level. Therefore, the contribution of first eigenenergy to the total charge density increases rapidly while that of higher eigenenergies decreases drastically as electric field increases i.e. with increasing electric field, total charge density resembles more and more to the increasing trend of charge density plot for first eigenstate overshadowing the decreasing trend of those plots for higher eigenstates. Moreover, it is seen that with increasing electric field the asymptotic eigenstates are closer to the Fermi level than the conventional eigenstates and hence, the above-mentioned effects are more prominent in asymptotic condition.

Fig. 4.6 shows the total inversion charge density variation. It is seen that the total charge density plots resembles to those for first eigenstate as expected. It is also observed that at higher surface electric field the plots approach closer to the interface with their peak increased and span decreased and the peak is seen higher in asymptotic condition. Therefore, the inversion charge density, ρ_{inv} and the inversion carrier density, N_{inv} is higher for higher electric field. A closer look also reveals that for a fixed surface electric field, the asymptotic plot is closer to the interface by about 2 \AA than the conventional plot with same span for both plots but with higher peak in asymptotic condition.

DC inversion charge centroid shift from the interface, X_{DC} can be calculated

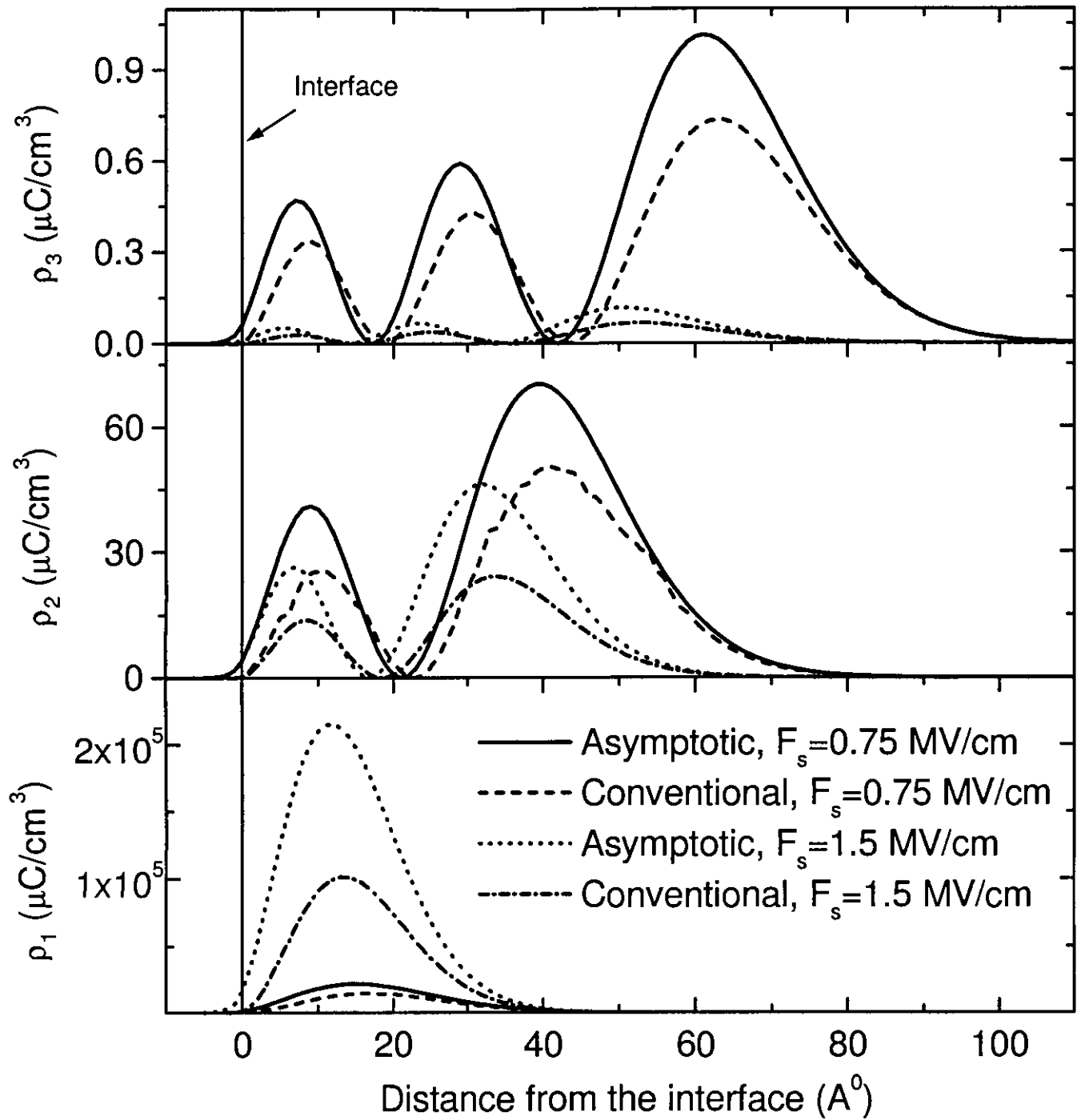


Figure 4.4: Inversion charge density for three lowest eigenenergies for both boundary conditions with $F_s = 0.75$ MV/cm and 1.5 MV/cm. Doping concentration = $5 \times 10^{17} \text{ cm}^{-3}$, Oxide thickness = 20 \AA , $T = 300^\circ \text{ K}$. The interface is at 0 \AA .

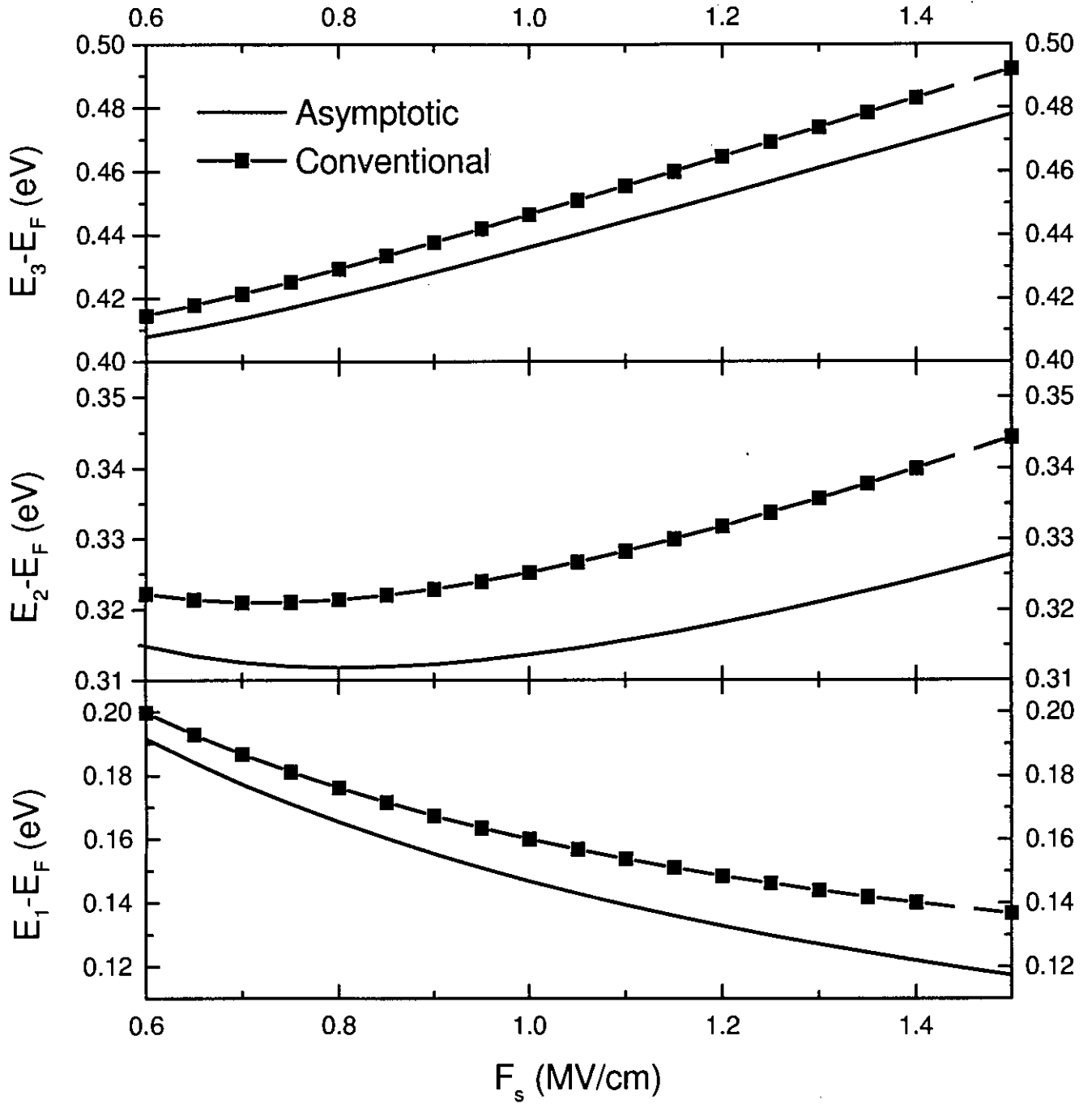


Figure 4.5: Variation of three lowest eigenenergies with respect to Fermi energy level against surface electric field, F_s , for both boundary conditions. Doping concentration = $5 \times 10^{17} \text{ cm}^{-3}$, Oxide thickness = 20 \AA , $T = 300^0 \text{ K}$.

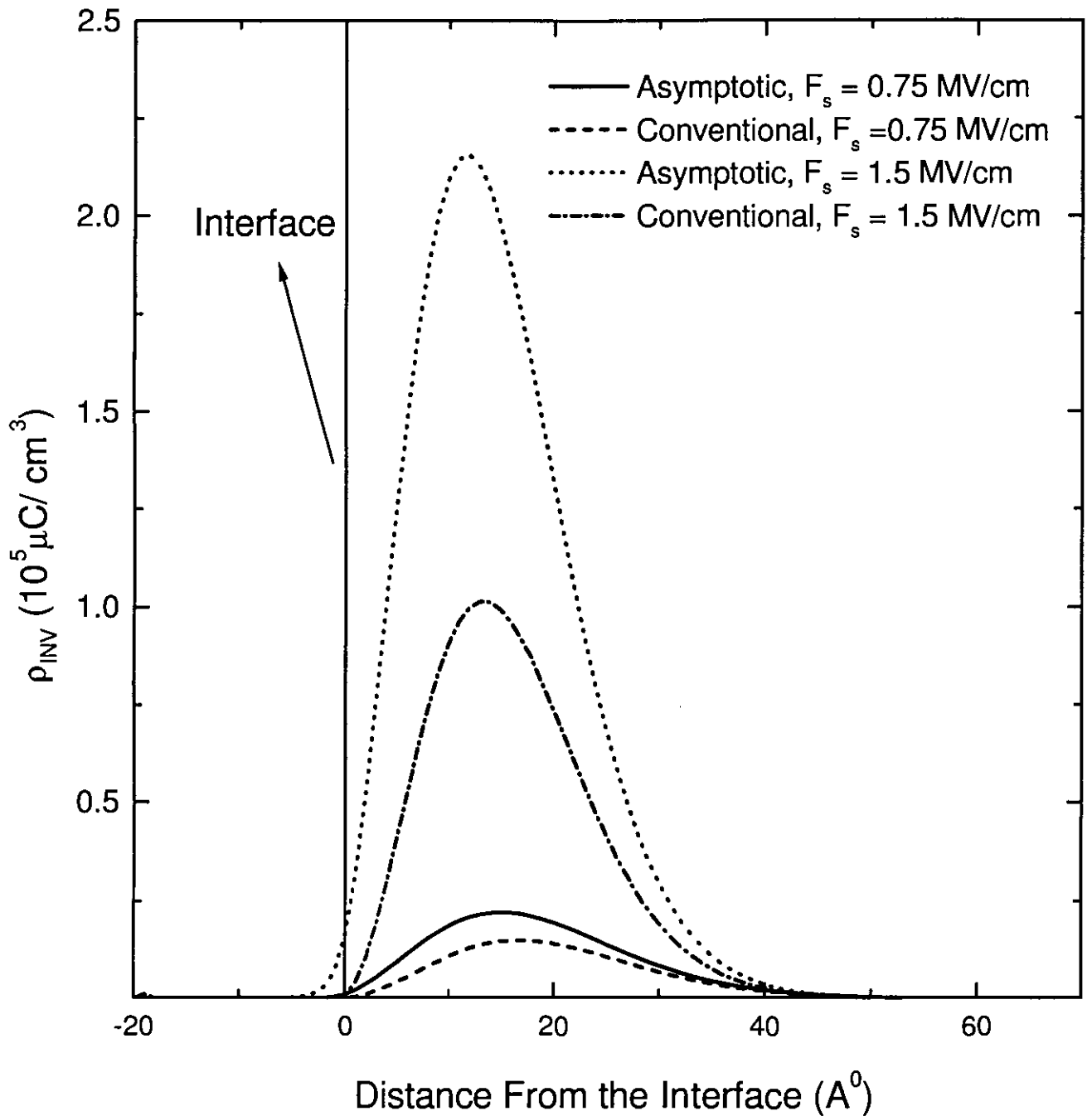


Figure 4.6: Total Inversion charge density for both boundary conditions with $F_s = 0.75 \text{ MV/cm}$ and 1.5 MV/cm . Doping concentration $= 5 \times 10^{17} \text{ cm}^{-3}$, Oxide thickness $= 20 \text{ \AA}$, $T = 300^\circ \text{ K}$. The interface is at 0 \AA

using Eq. 2.45. From this equation it is seen that X_{DC} is the distance of the centroid of the inversion charge density plot measured from the interface. Hence, the value of X_{DC} depends on the span of inversion charge density plot and also on how closer to the interface this plot is. Hence a study of Fig. 4.6 reveals that about 2 Å lower value of X_{DC} should be found for asymptotic condition than for conventional condition for all electric fields and at higher electric field, the value of X_{DC} for both boundary conditions should be decreased. All these results are tabulated in Table 4.2. It is noteworthy that although X_{DC} decreases with increasing electric field (i.e. with increasing degree of restriction applied to the quantum well) for both boundary conditions, the difference between the asymptotic X_{DC} and conventional X_{DC} remains unaffected.

Due to QM effects, the gate capacitance is corrected by a factor, X_{DC} as included in the Eqs. 2.46 and 2.47. This correction factor increases the gate oxide thickness by about one third of X_{DC} and hence decreases the value of effective gate capacitance. Since, conventional X_{DC} is higher than asymptotic X_{DC} , the asymptotic C_{EFF} is higher than the conventional C_{EFF} . Again, with higher electric field, as X_{DC} decreases, C_{EFF} is expected to increase. These results are summarized in Table 4.3.

From the above discussion it can be argued that the choice of appropriate boundary condition is important for deep submicron devices, as for such devices the change of effective gate oxide thickness and hence, effective gate capacitance due to asymptotic boundary condition compared with the conventional boundary condition can no longer be neglected.

4.3 Effects of Variation of Oxide Thickness

This section presents the results of the effects of variation of oxide thickness on QM calculations and compares the asymptotic results with conventional results.

| F_s (MV/cm) | Asymptotic, (\AA) | Conventional, (\AA) |
|---------------|------------------------------|--------------------------------|
| 0.75 | 17.96 | 19.58 |
| 1.50 | 13.93 | 15.61 |

Table 4.2: Calculated DC charge centroid shift from the interface, X_{DC} for both boundary conditions with $F_s = 0.75$ MV/cm and 1.5 MV/cm. Doping concentration, $N_A = 5 \times 10^{17} \text{ cm}^{-3}$, Oxide thickness, $T_{OX} = 20 \text{ \AA}$, $T = 300^0 \text{ K}$.

| F_s (MV/cm) | Asymptotic, ($\mu\text{F}/\text{cm}^2$) | Conventional, ($\mu\text{F}/\text{cm}^2$) |
|---------------|---|---|
| 0.75 | 1.33 | 1.30 |
| 1.50 | 1.40 | 1.37 |

Table 4.3: Calculated effective gate capacitance, C_{EFF} for both boundary conditions with $F_s = 0.75$ MV/cm and 1.5 MV/cm. Doping concentration, $N_A = 5 \times 10^{17} \text{ cm}^{-3}$, Oxide thickness, $T_{OX} = 20 \text{ \AA}$, $T = 300^0 \text{ K}$.

For this, oxide thickness is varied from 15 \AA to 30 \AA . The calculations are done for three doping densities: $1 \times 10^{17} \text{ cm}^{-3}$, $5 \times 10^{17} \text{ cm}^{-3}$ and $10 \times 10^{17} \text{ cm}^{-3}$. In all cases, potential profile is chosen at the onset of strong inversion.

With increasing oxide thickness, X_{DC} shows no variation at all for both boundary conditions for all three doping densities. In all cases, asymptotic X_{DC} is found lower than the conventional counterpart by about 2 \AA as expected. Since, increase of doping density increases the surface electric field (Eq.2.42) X_{DC} decreases for both boundary conditions with increasing doping density. These results are also observed in Fig. 4.7. Some fluctuations of X_{DC} calculated with conventional boundary condition are due to numerical instability of the program and has no physical significance.

Since T_{EFF} increases with increasing gate oxide thickness, T_{OX} (Eq. 2.46), C_{EFF} is expected to be decreasing with increasing T_{OX} (Eq. 2.47). Fig. 4.8 supports this point. This figure also shows that asymptotic C_{EFF} is higher than conventional C_{EFF} as expected. It is also seen that the change of asymptotic C_{EFF} with respect to conventional C_{EFF} increases with decreasing T_{OX} . This is explained with the fact that at $T_{OX} = 30 \text{ \AA}$, a 2 \AA difference between the

asymptotic X_{DC} and the conventional X_{DC} causes no significant change in T_{EFF} and hence, in C_{EFF} , but this change in those physical parameters is significantly increased for asymptotic condition when $T_{OX} \leq 20 \text{ \AA}$. From this Figure, the effect of doping densities on C_{EFF} is also observed. The figure shows that C_{EFF} increases for both boundary conditions with increasing doping density, as expected. This figure also shows that with increasing doping density, for same oxide thickness, the change in C_{EFF} due to asymptotic condition compared with conventional condition remains almost unaffected. This is due to the fact that for constant T_{OX} , a constant 2 \AA difference of X_{DC} found between the boundary conditions cause no significant change when doping density is increased.

Figs. 4.7 and 4.8 illustrate that the significance of the appropriate choice of boundary conditions become increasingly important as the device is scaled down. Again, for same oxide thickness, the choice of appropriate boundary condition has no significant effects when doping density is increased.

4.4 Effects of Variation of Surface Electric Field

This section presents the effects on the physical quantities for both the boundary conditions due to variation of surface electric field with three doping concentrations: $1 \times 10^{17} \text{ cm}^{-3}$, $5 \times 10^{17} \text{ cm}^{-3}$ and $10 \times 10^{17} \text{ cm}^{-3}$. Here, oxide thickness is chosen as 20 \AA . Surface electric field is varied from 0.6 MV/cm to 1.5 MV/cm . While varying this field, the device is operating from the onset of strong inversion to deep into the strong inversion.

With increasing electric field, the amount of band bending increases (Section 4.2), thus causing eigenenergies to be raised at a higher level. Figs. 4.9, 4.10 and 4.11, plotted with respect to the Si surface potential energy, show that eigenenergies increase with increasing electric field. From all these Figures, it is seen that the increase is slightly nonlinear and increases more rapidly at higher

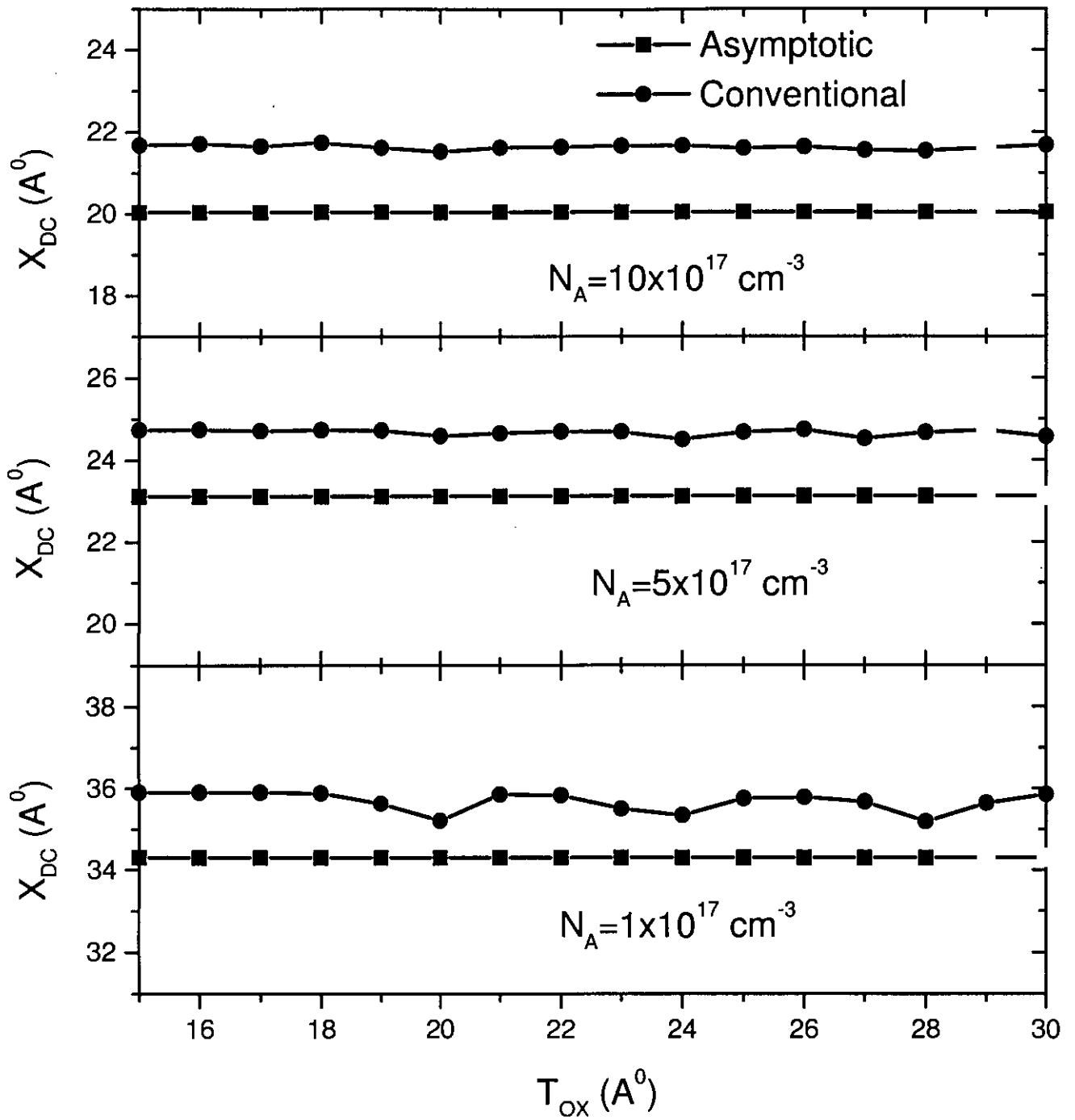


Figure 4.7: DC Charge Centroid shift from the interface, X_{DC} vs. Oxide Thickness, T_{OX} , with Doping Concentrations, $N_A = 1 \times 10^{17} \text{ cm}^{-3}$, $N_A = 5 \times 10^{17} \text{ cm}^{-3}$ and $N_A = 10 \times 10^{17} \text{ cm}^{-3}$. $T = 300^0\text{K}$.

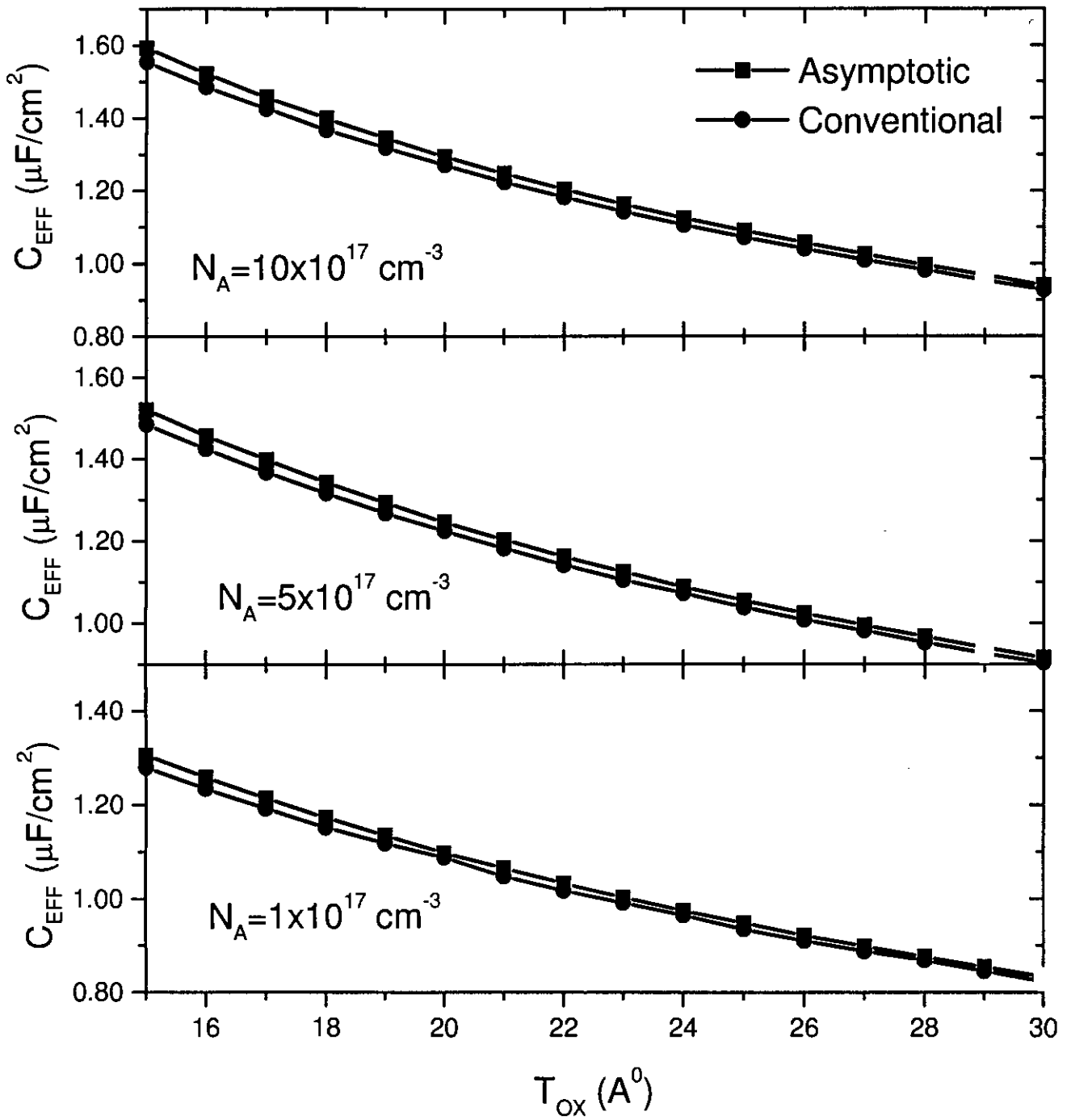


Figure 4.8: Effective gate oxide capacitance, C_{EFF} vs. Oxide Thickness, T_{OX} , with Doping Concentrations, $N_A = 1 \times 10^{17} \text{ cm}^{-3}$, $N_A = 5 \times 10^{17} \text{ cm}^{-3}$ and $N_A = 10 \times 10^{17} \text{ cm}^{-3}$. $T = 300^{\circ}\text{K}$.

electric field. In all these Figures, it is also seen that conventional eigenenergies are higher than the asymptotic eigenenergies and increase in doping density results in higher eigen values.

When surface electric field is increasing, inversion carrier density per unit area (N_{inv}) increases by more than one order of magnitude as shown in Fig. 4.12. From this plot it is seen that with increasing electric field N_{inv} is higher and increases more rapidly for asymptotic condition than for conventional condition as expected from the explanation in Section 4.2. Also, the effect of doping density is observed. Since, F_s is proportional to the sum of depletion layer charge density, $N_A z_d$ (where, z_d is the depletion layer thickness) and inversion layer charge density, N_{inv} (Eqs. 2.42, 2.43, 2.44), for a given F_s higher doping density results in lower N_{inv} . This fact is reflected in the Fig. 4.12.

Fig. 4.13 shows the effects of increasing surface electric field on X_{DC} for three doping densities. From the figure, X_{DC} is found decreasing while F_s is increasing in all cases. In this figure, again an about 2 Å difference is observed between the two boundary conditions and asymptotic X_{DC} is found lower than the conventional X_{DC} . These results are in consistent with the discussion presented in Section 4.2. The insignificant effect of doping density on X_{DC} is due to the fact that X_{DC} depends on the degree of restriction applied to the quantum well, which increases when surface electric field increases. For a fixed surface electric field, increase of doping density causes no change on the degree of restriction and hence no change in X_{DC} values for both boundary conditions is observed in Fig. 4.13.

From the reference of discussion presented in Section 4.2 it is expected that with increasing electric field effective gate capacitance, C_{EFF} increases for both boundary conditions and the asymptotic C_{EFF} is higher than the conventional C_{EFF} . Fig. 4.14 reflects these facts for all doping densities. A closer look into this figure shows that the asymptotic C_{EFF} increases more rapidly than the con-

ventional C_{EFF} , for a fixed doping density. This is because of the fact that a 2 Å difference in X_{DC} for $F_s = 150 \text{ MV/cm}$ causes more significant change in T_{EFF} and hence, in C_{EFF} than that for $F_s \leq 90 \text{ MV/cm}$. This figure also depicts the insignificant effect of doping density variation on C_{EFF} . Here the explanation is that, for same surface electric field and for same device oxide thickness, increase of doping density causes no change in X_{DC} for both boundary conditions and also in the difference of X_{DC} between the two boundary conditions.

The above discussion argues that the choice of appropriate boundary condition for deep submicron devices is increasingly important when surface electric field is increasing, but is not significant with increasing doping density keeping surface electric field constant. In other words, a submicron device when operates in deep strong inversion region, the choice of appropriate boundary condition is important for accurate modeling.

4.5 Effects of Variation of Gate Voltage

Gate voltage is related to surface electric field, as seen from the Eq. 2.50. Hence, variation of surface electric field means variation of gate voltage. Here, oxide thickness is chosen as 20 Å; three doping densities are chosen: $1 \times 10^{17} \text{ cm}^{-3}$, $5 \times 10^{17} \text{ cm}^{-3}$ and $10 \times 10^{17} \text{ cm}^{-3}$. While varying this voltage, the device is operating from the onset of strong inversion to deep into the strong inversion.

Figs. 4.15, 4.16 and 4.17 show that the effects of V_G on N_{inv} , X_{DC} and C_{EFF} that are similar to surface electric field variation (see Figs. 4.12, 4.13 and 4.14). The effects of doping density are also insignificant in these plots, except that increasing doping density results in a decreasing gate voltage. This is explained with the help of Eq. 2.50 and Fig. 4.1. For a given F_s , the first term in Eq. 2.50 varies slightly (since ϕ_F depends logarithmically on N_A) and the third term remains unchanged (Eq. 2.42) with respect to change in the doping density.

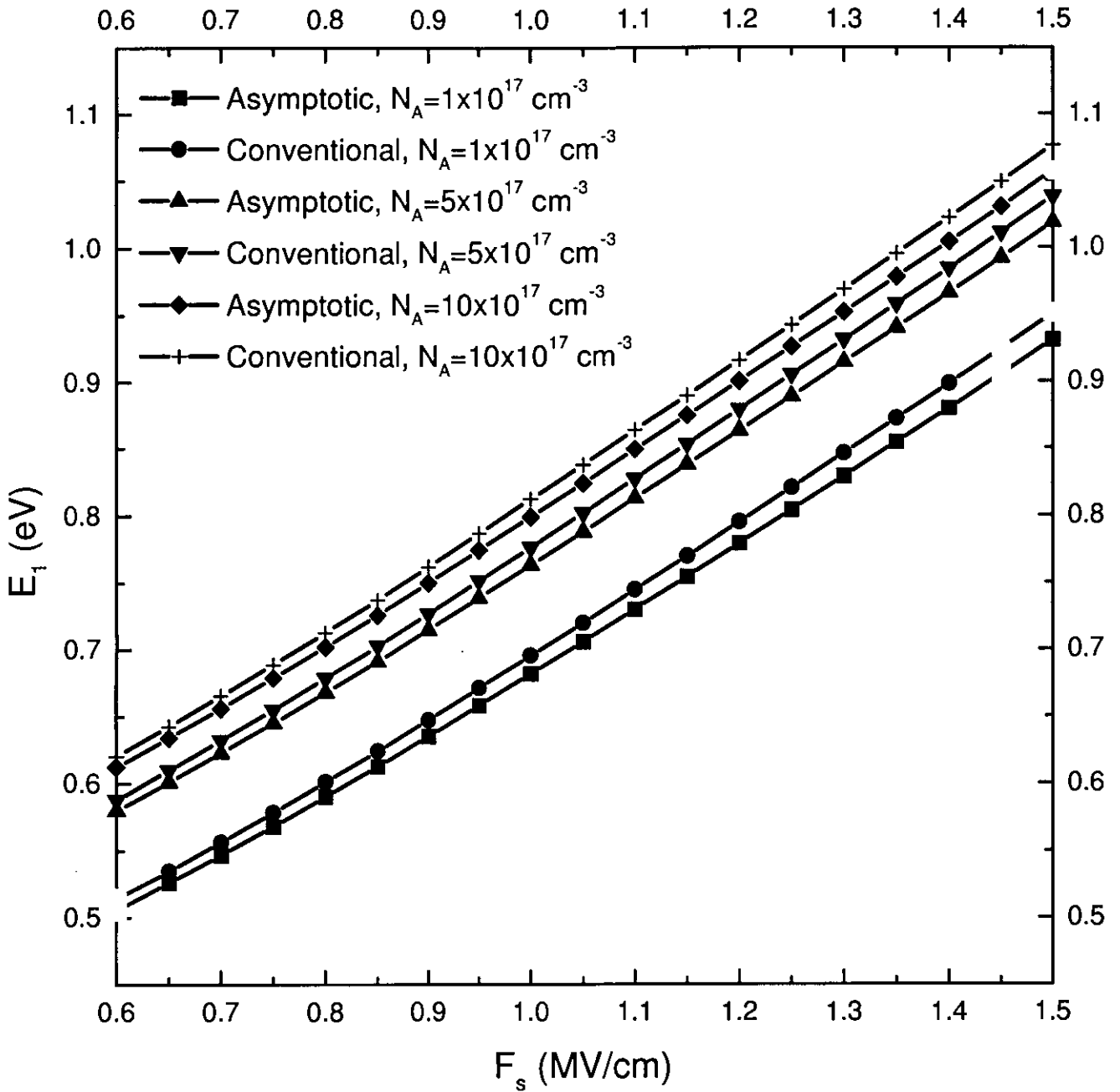


Figure 4.9: First eigenenergy with respect to Si potential energy at the interface, E_1 vs. Surface Electric Field, F_s , with Doping Concentrations, $N_A = 1 \times 10^{17} \text{ cm}^{-3}$, $N_A = 5 \times 10^{17} \text{ cm}^{-3}$ and $N_A = 10 \times 10^{17} \text{ cm}^{-3}$. $T = 300^0 \text{ K}$.

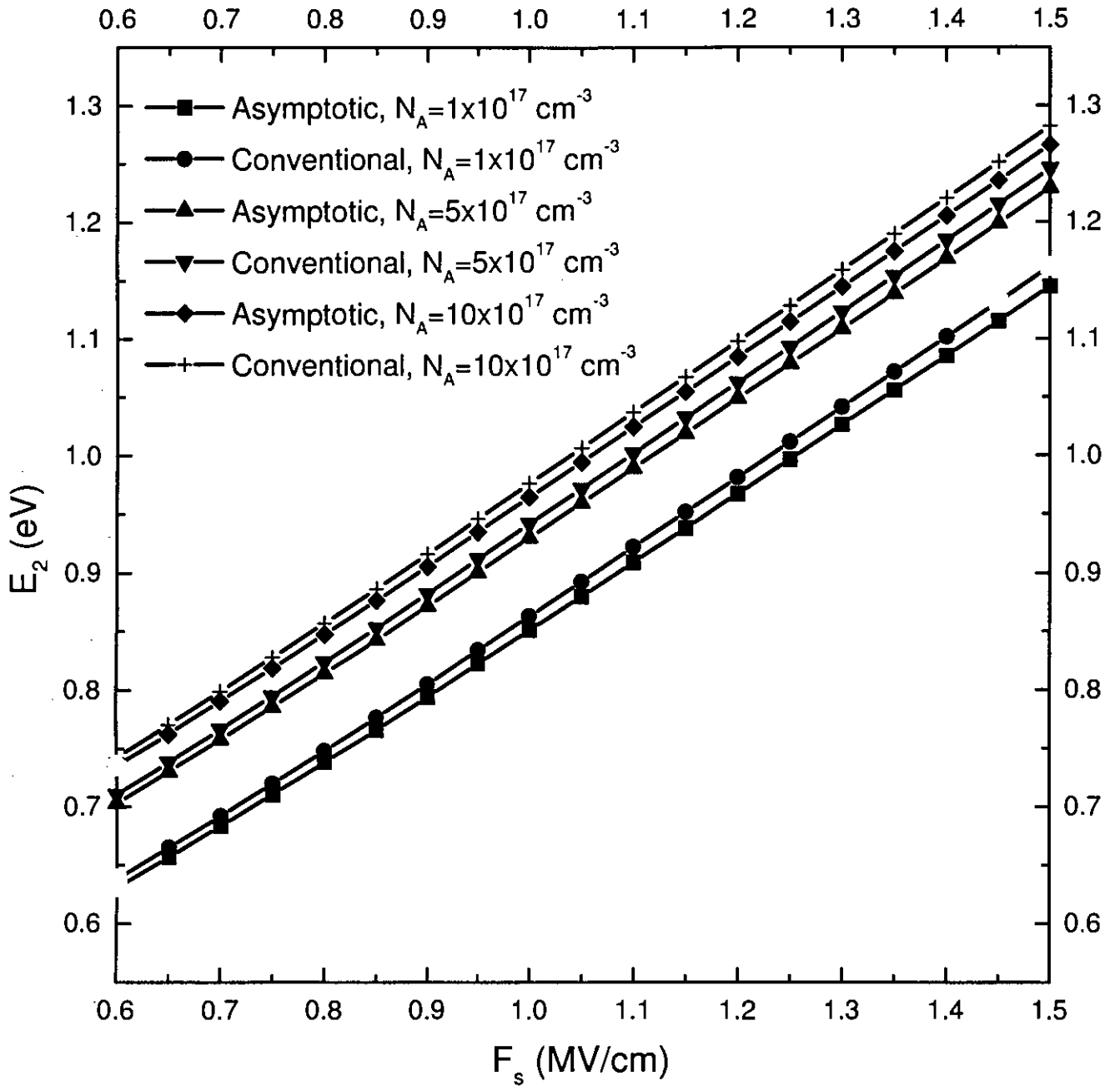


Figure 4.10: Second eigenenergy with respect to Si potential energy at the interface, E_2 vs. Surface Electric Field, F_s , with Doping Concentrations, $N_A = 1 \times 10^{17} \text{ cm}^{-3}$, $N_A = 5 \times 10^{17} \text{ cm}^{-3}$ and $N_A = 10 \times 10^{17} \text{ cm}^{-3}$. $T = 300^0 \text{ K}$.

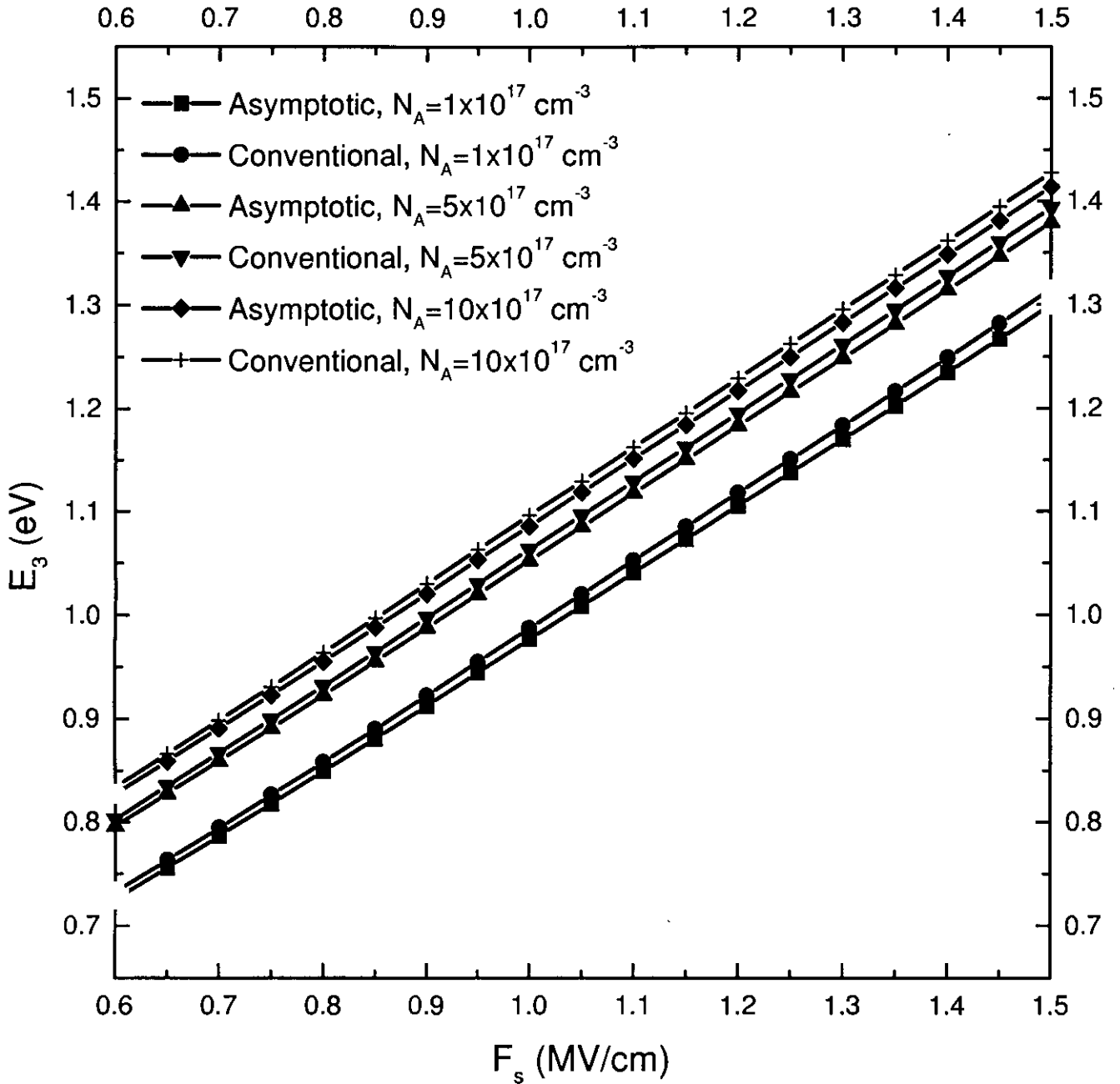


Figure 4.11: Third eigenenergy with respect to Si potential energy at the interface, E_3 vs. Surface Electric Field, F_s , with Doping Concentrations, $N_A = 1 \times 10^{17} \text{ cm}^{-3}$, $N_A = 5 \times 10^{17} \text{ cm}^{-3}$ and $N_A = 10 \times 10^{17} \text{ cm}^{-3}$. $T = 300^0 \text{ K}$.

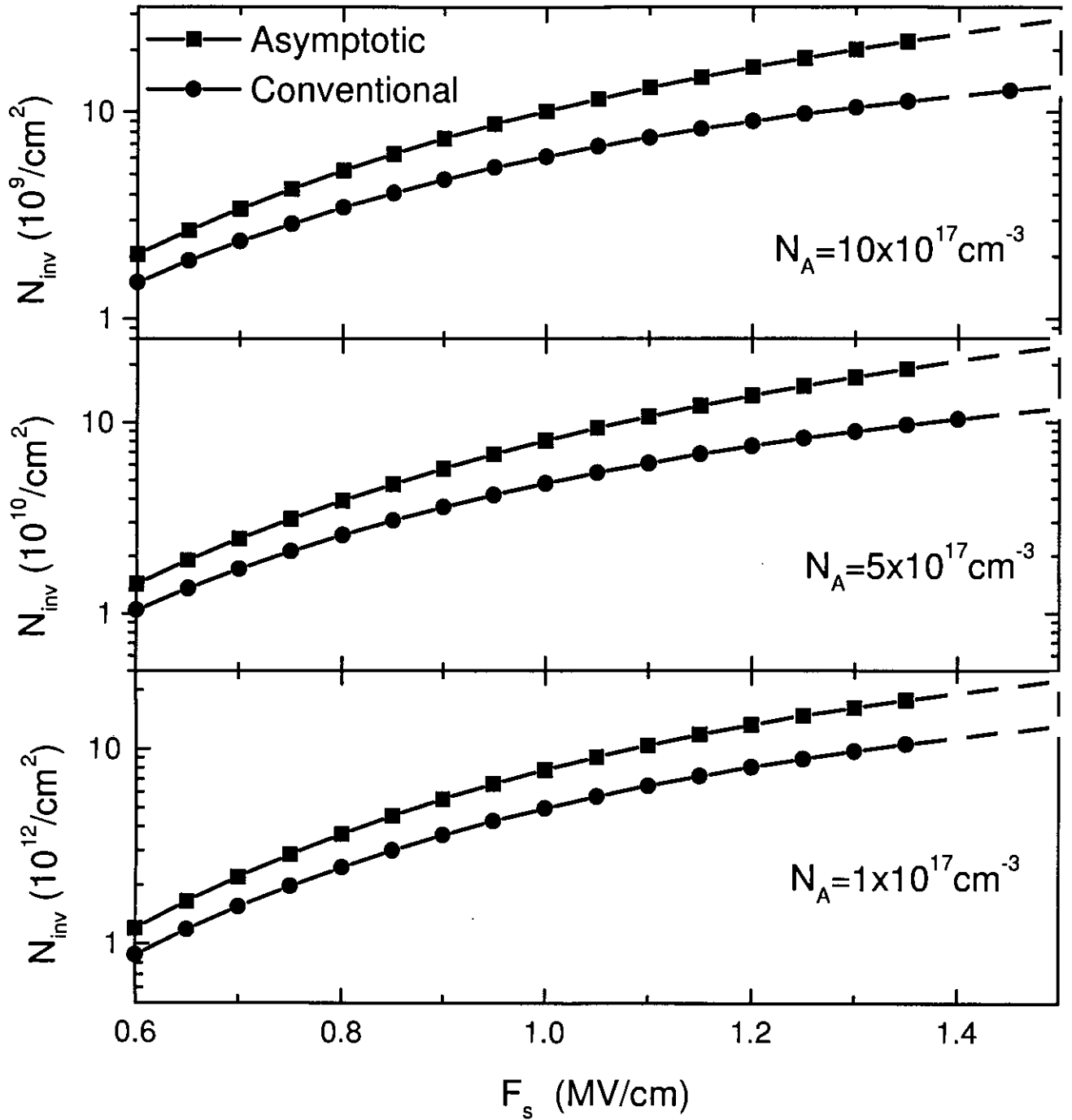


Figure 4.12: Inversion Charge Carrier Density, N_{inv} vs. Surface Electric Field, F_s , with Doping Concentrations, $N_A = 1 \times 10^{17} \text{ cm}^{-3}$, $N_A = 5 \times 10^{17} \text{ cm}^{-3}$ and $N_A = 10 \times 10^{17} \text{ cm}^{-3}$. $T = 300^{\circ} \text{ K}$.

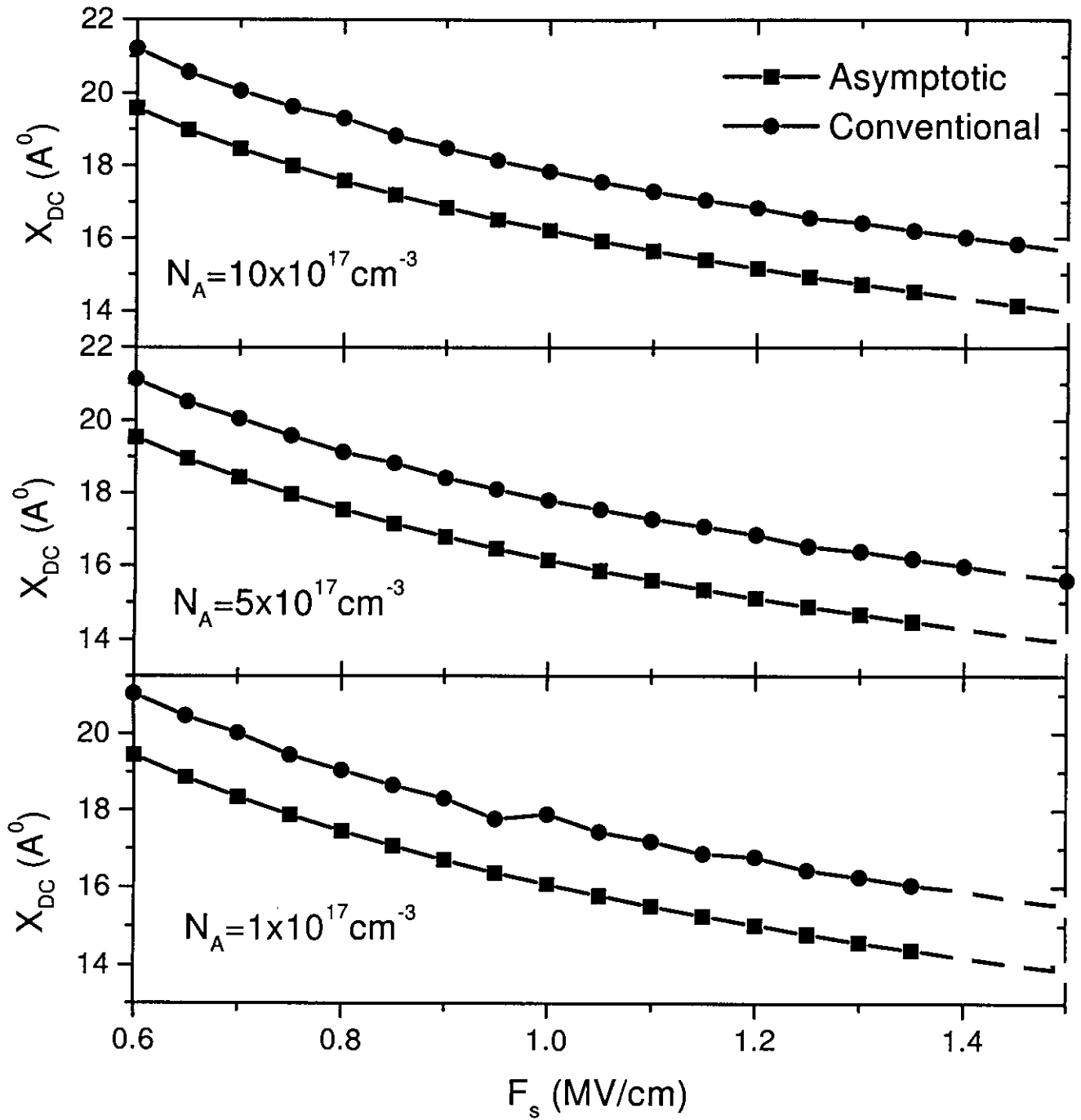


Figure 4.13: DC Charge Centroid Shift from the interface, X_{DC} vs. Surface Electric Field, F_s , with Doping Concentrations, $N_A = 1 \times 10^{17} \text{ cm}^{-3}$, $N_A = 5 \times 10^{17} \text{ cm}^{-3}$ and $N_A = 10 \times 10^{17} \text{ cm}^{-3}$. $T = 300^{\circ} \text{ K}$.

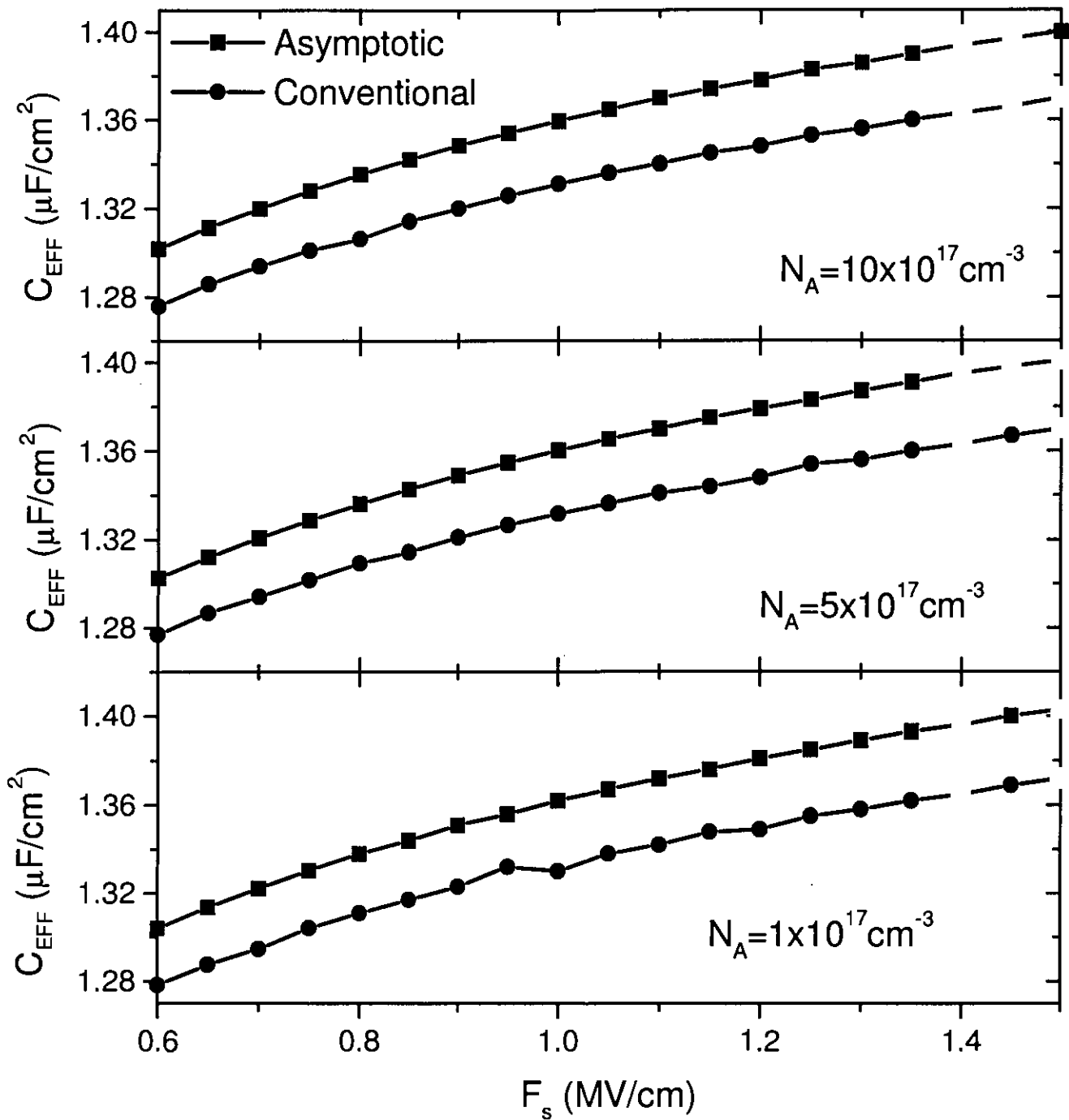


Figure 4.14: Effective Gate Capacitance, C_{EFF} vs. Surface Electric Field, F_s , with Doping Concentrations, $N_A = 1 \times 10^{17} \text{ cm}^{-3}$, $N_A = 5 \times 10^{17} \text{ cm}^{-3}$ and $N_A = 10 \times 10^{17} \text{ cm}^{-3}$. $T = 300^0 \text{ K}$.

However, Fig. 4.1 shows a reduction in ϕ_s (second term in Eq. 2.50) with increasing doping density. As a consequence, V_G is smaller for higher doping density corresponding to a fixed surface electric field.

Due to the variation of gate voltage the same argument given for the effects on the choice of appropriate boundary condition due to variation of surface electric field holds true.

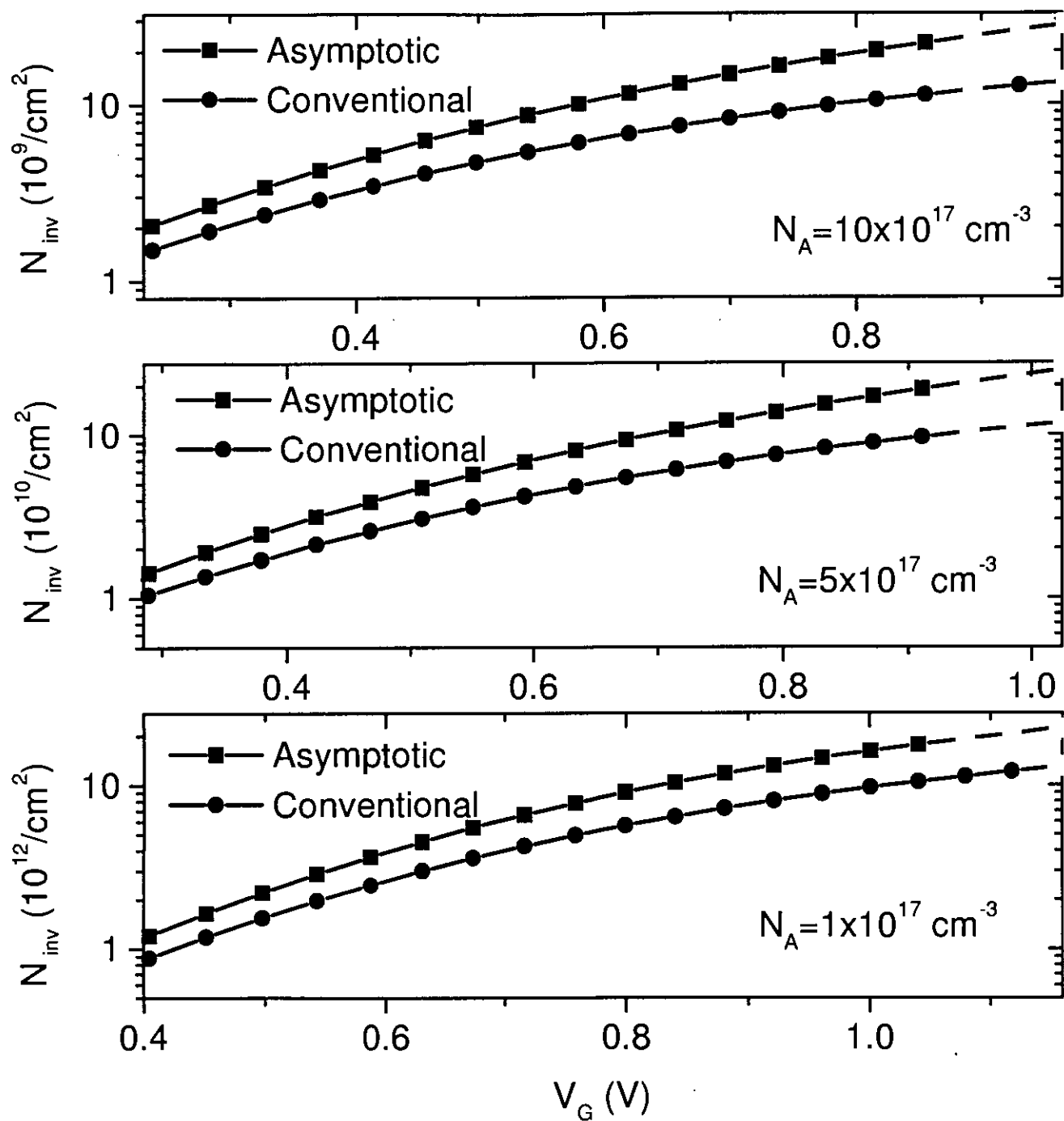


Figure 4.15: Inversion Charge Carrier Density, N_{inv} vs. Gate Voltage, V_G , with Doping Concentrations, $N_A = 1 \times 10^{17} \text{ cm}^{-3}$, $N_A = 5 \times 10^{17} \text{ cm}^{-3}$ and $N_A = 10 \times 10^{17} \text{ cm}^{-3}$. $T = 300^0 \text{ K}$.

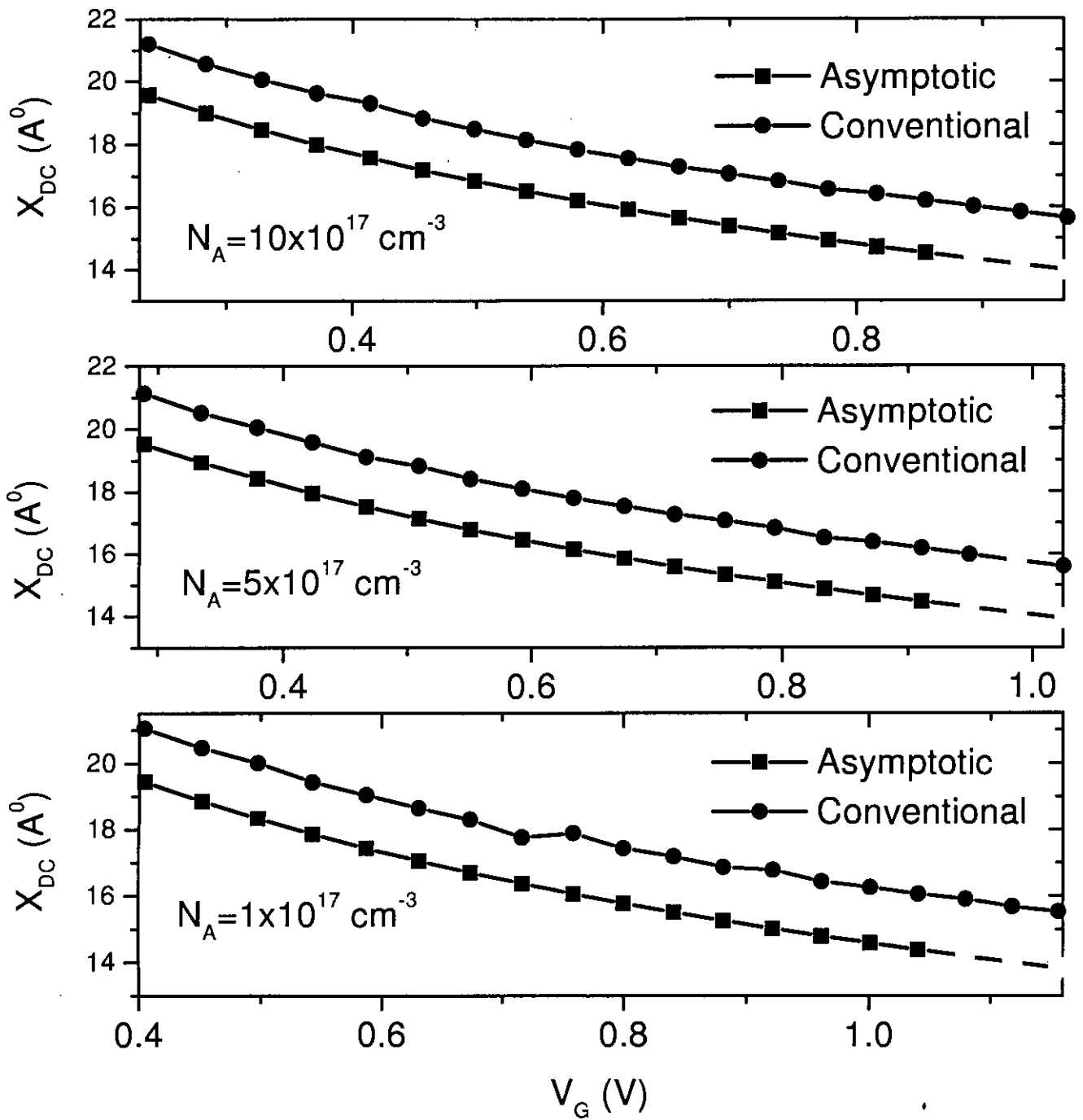


Figure 4.16: DC Charge Centroid Shift from the interface, X_{DC} vs. Gate Voltage, V_G , with Doping Concentrations, $N_A = 1 \times 10^{17} \text{ cm}^{-3}$, $N_A = 5 \times 10^{17} \text{ cm}^{-3}$ and $N_A = 10 \times 10^{17} \text{ cm}^{-3}$. $T = 300^{\circ} \text{ K}$.

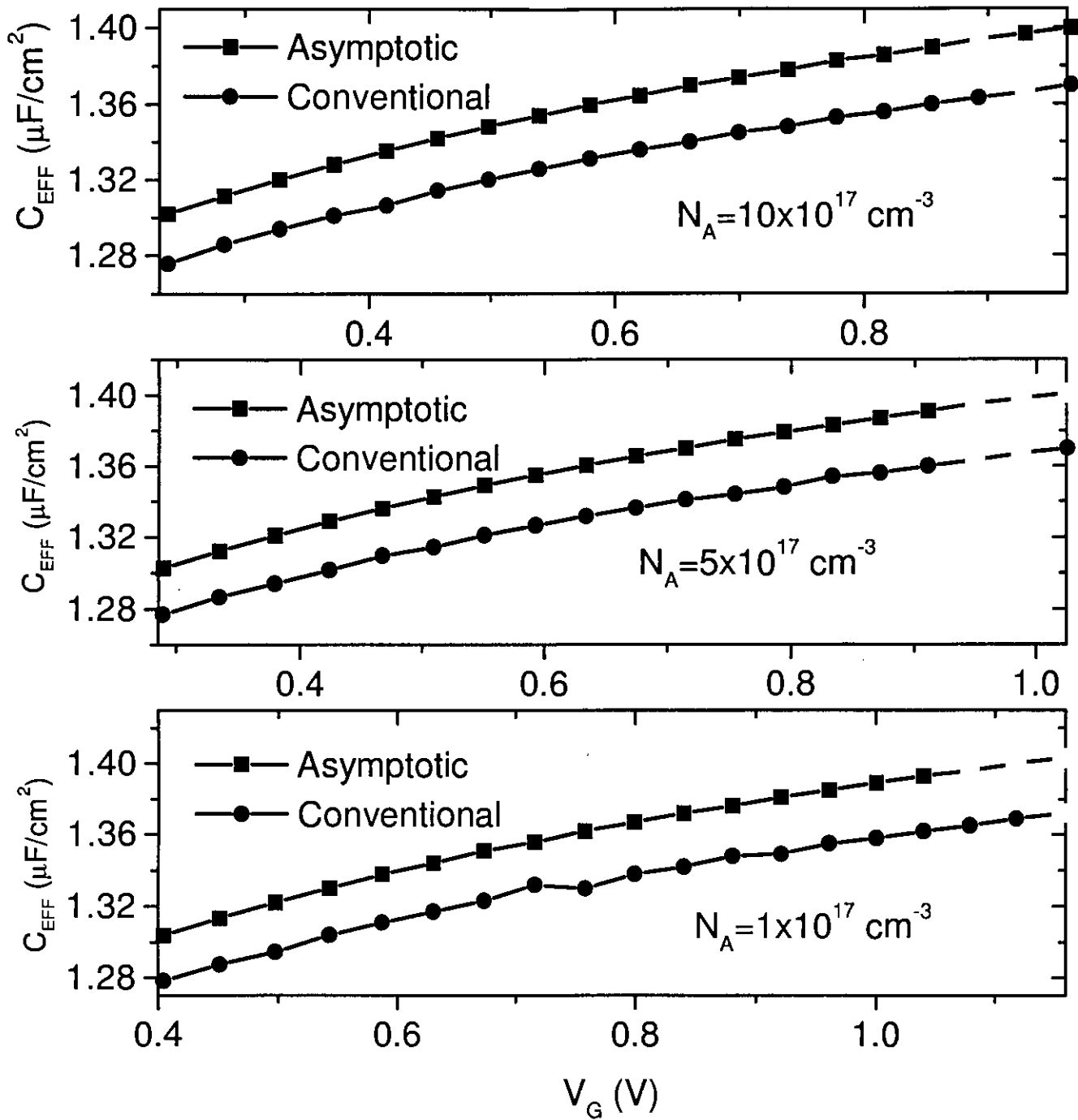


Figure 4.17: Effective Gate Capacitance, C_{EFF} vs. Gate Voltage, V_G , with Doping Concentrations, $N_A = 1 \times 10^{17} \text{ cm}^{-3}$, $N_A = 5 \times 10^{17} \text{ cm}^{-3}$ and $N_A = 10 \times 10^{17} \text{ cm}^{-3}$. $T = 300^\circ \text{ K}$.

Chapter 5

CONCLUSION

99612

The quantization effects in MOS inversion layer using a new boundary condition as well as the conventional boundary condition are studied, and a comparative study of the effects of these boundary conditions is made in this work.

5.1 Discussion

In the study of quantization effects in MOS inversion layer, conventionally the wavefunction penetration inside the oxide region is neglected. Since the present MOS devices approach the deep submicron dimensions, this boundary condition is no longer justified. Hence, a new boundary condition which encounters the wavefunction penetration is introduced. In this work both these boundary conditions are employed in calculation of eigenenergies, normalized wavefunctions, inversion charge density (N_{inv}), DC charge centroid shift from the oxide-semiconductor interface (X_{DC}) and effective gate oxide capacitance (C_{EFF}). A comparative study of the effects of these boundary conditions made in this work suggests that the choice of boundary condition for deep submicron devices is significant. Results show that the choice becomes increasingly more important as the devices are scaled down, i.e. as the oxide thickness is decreased and the surface electric field is increased.

5.2 Suggestions for Future Work

In the present analysis, exponential potential profile is assumed instead of actual potential distribution. Moreover, the potential profile is assumed to be known i.e. self-consistency is not used. Another assumption of this work is that an ideal device is chosen, that is no interface charge is present and no scattering processes are associated with this device. All these assumptions make the analysis simple so that a quick insight can be made into whether the asymptotic boundary condition

is more justified over the conventional boundary condition.

The scope of a complete research requires an extensive study considering not only the self-consistency, but also the actual device condition. After that, all the operating regions should be considered. Though the work verifies the need to use asymptotic boundary condition in calculating inversion charge density, DC charge centroid and gate capacitance, the verification should be made for other quantities such as the threshold voltage and gate leakage current. Scattering processes and interface charges may be included in the simulation to make the results more meaningful.

Bibliography

- [1] Scott A. Hareland, S. Krishnamurthy, S. Jallepalli, C. Yeap, Khaled Hasnat, Al F. Tasch and C. M. Maziar, "A computationally efficient model for inversion layer quantization effects in deep submicron N-channel MOS-FETs", *IEEE Trans. on Electron Devices*, vol. 43, pp. 90-95, 1996.
- [2] "The national Technology roadmap for Semiconductors: Technology Needs", Semiconductor Industry Association, San Jose, California, 1997.
- [3] F. Stern and W.E. Howard, "Properties of semiconductor surface inversion layers in the electric quantum limit", *Phys. Rev.*, vol.163, pp. 816-835, 1967.
- [4] F. Stern, "Self-consistent results for n-type Si inversion layers", *Phys. Rev. B*, vol.5, pp. 4891-4899, 1972.
- [5] C. Moglestue, "Self-consistent calculation of electron and hole inversion charges at silicon-silicon dioxide interfaces", *J. Appl. Phys.*, vol. 59, pp. 3175-3183, 1986.
- [6] Y. Ohkura, "Quantum effects in Si n-MOS inversion layer at high substrate concentration", *Solid-State Electronics*, vol. 33, pp. 1581-1585, 1990.
- [7] G. Paasch, S. Scheinert and K. Tarnay, "Influence of inversion channel quantisation on the surface potential in the MOS structure", *Phys. Stat. Sol.*, vol. 149, pp. 751-755, 1995.

- [8] S. Takagi and A. Toriumi, "Quantitative understanding of inversion-layer capacitance in Si-MOSFETs", IEEE Trans. Electron Devices, vol. 42, pp. 2125-2130, 1995.
- [9] Samar Saha, "Effects of inversion layer quantization on channel profile engineering for NMOSFETs with $0.1\mu m$ channel lengths", Solid-State Electronics, vol. 42, pp. 1985-1991, 1998.
- [10] C. Fiegna and A. Abramo, "Analysis of quantum effects in nonuniformly doped MOS structures", IEEE Trans. Electron Devices, vol. 45, pp. 877-880, 1998.
- [11] Y-C King, H. Fujioka, S. Kamohara, K. Chen and C. Hu, "DC electrical oxide thickness model for quantization of the inversion layer in MOSFET's", Semicond. Sci. Technol., vol. 13, pp. 963-966, 1998.
- [12] W. Liu, X. Jin, Y. King and C. Hu, "An efficient and accurate compact model for thin-oxide-MOSFET intrinsic capacitance considering the finite charge layer thickness", IEEE Trans. on Electron Devices, vol. 46, pp. 1070-1072, 1999.
- [13] A. Pacelli, A. S. Spinelli and L. M. Perron, "Carrier quantization at flat bands in MOS devices", IEEE Trans. on Electron Devices, vol. 46, pp. 383-387, 1999.
- [14] M. J. van Dort, P. H. Woerlee, A. J. Walker, "A simple model for quantization effects in heavily-doped silicon MOSFETs at inversion conditions", Solid-State Electron., vol. 37, pp. 411-414, 1994.
- [15] W-K Shih, E. X. Wang, S. Jallepalli, F. Leon, C. M. Maziar and A. F. Tasch, "Modeling gate leakage current in nMOS structures due to tunneling

- through an ultra-thin oxide”, *Solid-State Electron.*, vol. 42, pp. 997-1006, 1998.
- [16] C-K Huang, W. E. Zhang and C. H. Yang, “Two-dimensional numerical simulation of schottky barrier MOSFET with channel length to 10 nm”, *IEEE Trans. Electron Devices*, vol. 45, pp. 842-848, 1998.
- [17] C-H Choi, J-S Goo, T-Y Oh, Z. Yu, R. W. Dutton, A. Bayoumi, M. Cao, P. V. Voorde, D. Vook and C. H. Diaz, “MOS C-V characterization of ultrathin gate oxide thickness (1.3-1.8 nm)”, *IEEE Trans. Electron Devices*, vol. 20, pp. 292-294, 1999.
- [18] A. S. Spinelli, A. Benvenuti, S. Villa, A. L. Lacaita, “MOSFET simulation with quantum effects and nonlocal mobility model”, *IEEE Trans. Electron Devices*, vol. 20, pp. 298-300, 1999.
- [19] S. Takagi, M. Takayanagi and A. Toriumi, “Characterization of inversion-layer capacitance of holes in Si MOSFET’s”, *IEEE Trans. Electron Devices*, vol. 46, pp. 1446-1450, 1999.
- [20] S. Jallepalli, J. Bude, W.-K. Shih, M. R. Pinto, C. M. Maziar and A. F. Tasch, “Electron and hole quantization and their impact on deep submicron silicon p- and n-MOSFET characteristics”, *IEEE Trans. on Electron Devices*, vol. 44, pp. 297-302, 1997.
- [21] A. Haque, A. Rahman and I. B. Chowdhury, “On the use of appropriate boundary conditions to calculate the normalized wavefunctions in the inversion layers of MOSFET’s with ultra-thin gate-oxides”, *Solid-State Electron.*, vol. 44, pp. 1833-1836, 2000.

- [22] A. N. Khondker, M.R. Khan and A.F.M. Anwar, "Transmission line analogy of resonance tunneling phenomena: the generalized impedance concept", J. Appl. Phys., vol. 63, pp. 5191-5193, 1988.
- [23] A. Haque and A. N. Khondker, "An efficient technique to calculate the normalized wave functions in arbitrary one-dimensional quantum well structures", J. Appl. Phys., vol. 84, pp. 5802-5804, 1998.
- [24] Ben G. Streetman, "Solid-state electronic devices", Second edition, Prentice-Hall Inc., pp. 70-75, 300-312, 1980.
- [25] S. M. Sze, "Physics of semiconductor devices", Second edition, Wiley Eastern Limited, pp. 362-366, 1987.
- [26] Y. Tsvividis, "Operation and modeling of the MOS Transistor", McGraw-Hill, Ch.2, 1999.
- [27] Michael Shur, "Physics of semiconductor devices", Prentice-Hall Inc., pp. 332-335, 1990.
- [28] A. Haque and A. N. Khondker, "On the conductance and conductivity of disordered quantum wires", J. Appl. Phys., vol. 80, pp. 3876-3880, 1996.
- [29] N. Yang, W. K. Henson, J. R. Hauser and J. J. Wortman, "Modeling study of ultra thin gate oxides using direct tunneling current and capacitance-voltage measurements in MOS devices", IEEE Trans. electron Devices, vol. 46, pp. 1465-1470, 1999.

